The Journal of Chemical Physics ARTICLE scitation.org/journal/jcp

High harmonic spectra computed using time-dependent Kohn–Sham theory with Gaussian orbitals and a complex absorbing potential

Cite as: J. Chem. Phys. 156, 204123 (2022); doi: 10.1063/5.0079910
Submitted: 25 November 2021 • Accepted: 28 April 2022 •
Published Online: 31 May 2022

Ying Zhu and John M. Herbert[a)]

AFFILIATIONS

Department of Chemistry and Biochemistry, and Chemical Physics Graduate Program, The Ohio State University, Columbus, Ohio 43210, USA

[a)]Author to whom correspondence should be addressed: herbert@chemistry.ohio-state.edu

ABSTRACT

High harmonic spectra for H_2 and H_2^+ are simulated by solving the time-dependent Kohn–Sham equation in the presence of a strong laser field using an atom-centered Gaussian representation of the density and a complex absorbing potential. The latter serves to mitigate artifacts associated with the finite extent of the basis functions, including spurious reflection of the outgoing electronic wave packet. Interference between the outgoing and reflected waves manifests as peak broadening in the spectrum as well as the appearance of spurious high-energy peaks after the harmonic progression has terminated. We demonstrate that well-resolved spectra can be obtained through the use of an atom-centered absorbing potential. As compared to grid-based algorithms, the present approach is more readily extensible to larger molecules.

I. INTRODUCTION

The experimental study of molecules and materials under short, intense femtosecond and even attosecond laser pulses is becoming possible due to the advent of ultra-short pulse technology based on high harmonic generation (HHG).[1–4] This has enabled the development of soft x-ray and extreme ultraviolet laser pulses with ultrafast time resolution,[5–7] even in tabletop instruments,[8–10] which promises to make this technology more widely available in the near future. The strong-field phenomena that can be probed with this new generation of instruments pose challenges to well-developed theoretical models that work in the perturbative (weak-field) regime, as new phenomena arise in strong electric fields.[11,12] These include above-threshold ionization, non-sequential ionization, multiphoton ionization, delayed photoemission, and HHG.[12–16] Attosecond experiments[17] are expected to provide fundamental probes of electron correlation and ultrafast charge migration in both molecules and materials.[16–21] The theoretical description of this emergent physics promises to push the envelope of computational quantum chemistry.[22,23]

In the context of time-dependent density functional theory (TDDFT),[24–26] strong-field phenomena cannot be described within the linear-response approximation[27] that has become essentially synonymous with the moniker of TDDFT, at least within the quantum chemistry community.[28] In principle, an exact theory can still be formulated even in the strong-field or non-perturbative regime based on the direct solution of the time-dependent Kohn–Sham equation.[14,29] This approach is often called "real-time" TDDFT,[30–32] although we prefer the term *time-dependent Kohn–Sham* (TDKS) theory.[32–34] In practice, however, there are significant questions as to whether existing exchange–correlation functionals that invoke the adiabatic approximation are up to the task,[14,31] although improving the description of the derivative discontinuity improves the description of ionization, even within the adiabatic approximation.[35]

In the present work, we examine the HHG phenomenon in simple test cases, namely H_2^+ and H_2, using an atom-centered

Gaussian representation of the Kohn–Sham orbitals. Previous TDKS simulations of HHG in H_2 have emphasized the importance of using an exchange–correlation functional with correct asymptotic behavior.[36–39] In some calculations, this has been achieved using either time-dependent Hartree–Fock (TDHF) theory or else the closely related time-dependent configuration interaction singles (TD-CIS) method.[39–42] Functionals with an explicit self-interaction correction have also been employed,[36,37] as this helps with the aforementioned derivative discontinuity. Recently, the use of range-separated, "long-range corrected" (LRC) hybrid functionals[43–48] has been considered for the simulation of HHG in H_2 and other small molecules,[42] and for strong-field photoionization.[49,50] As compared to either generalized gradient approximations (GGAs) or even global hybrid functionals, LRC functionals do a much better job of approximating the derivative discontinuity.[51] The simulations presented herein will be based upon the LRC-ωPBE functional,[46] as in some previous simulations of HHG.[42]

Rather than using a grid-based algorithm to integrate either the time-dependent Schrödinger equation or the TDKS equation,[29,36,37,52–55] we follow the path established by Saalfrank, Luppi, and others[38–42,55–59] using atom-centered Gaussian basis sets to represent the density. This makes TDKS simulations accessible with widely available, general-purpose quantum chemistry codes, and the compactness of the Gaussian representation offers the possibility to extend TDKS calculations to larger molecules than are feasible in grid-based representations. Even for H_2, where both approaches are feasible, the Gaussian representation is found to be at least an order of magnitude more efficient,[38] meaning minutes instead of hours of computer time to obtain a spectrum.[55] Furthermore, only the Gaussian representation is scalable to larger molecules. This efficiency might be used, for example, to simulate HHG in liquids,[60] crystalline solids,[7,61] or nanostructured materials,[62–65] all of which have been realized experimentally. For HHG in liquids, the role of molecular disorder has been emphasized,[66] suggesting that model systems larger than a single molecule are required to understand this phenomenon.

That said, previous work on small-molecule HHG has emphasized the important role that is played by Rydberg and continuum states,[41,56,67] which is unsurprising given the role of tunneling ionization in the HHG process,[1,2,20,68] yet these states are not well described by standard Gaussian basis sets and very diffuse basis functions are required.[38,41,42,56] Even so, a strong laser field will push the electronic wave packet into regions of space where support from the atom-centered basis functions is waning, and this will manifest as spurious reflection of that wave packet by the artificial potential wall created by the lack of basis function support. To circumvent this problem, previous work on strong-field electron dynamics within an atom-centered Gaussian representation has employed a heuristic finite-lifetime model in which unbound states are given complex energies, corresponding to finite lifetimes.[40,41,56,57,69]

As an alternative, we replace the heuristic lifetime model with the machinery of a complex absorbing potential (CAP). Such potentials are often used for the description of metastable electronic states whose wave functions are not square-integrable.[70–72] CAPs are also used as absorbing boundary conditions in wave packet quantum dynamics calculations,[73] including grid-based simulations of strong-field electron dynamics.[36,53,67,74–76] The CAP is trivial to implement within a real-space grid representation of the wave function, but versions have also been developed for atom-centered Gaussian basis functions.[49,77–79] Atom-centered CAPs have been used to study strong-field ionization via TD-CIS (rather than TDKS) simulations,[53,76–86] because self-interaction error is known to significantly suppress the strong-field ionization rate.[29] To the best of our knowledge, however, it has not been demonstrated that HHG spectra can be simulated in this way, namely, using a combination of atom-centered Gaussian basis functions and an atom-centered CAP. HHG spectra have been simulated using TD-CIS simulations with Gaussian basis sets,[41,42,55–59] with heuristic lifetime models instead of a CAP. Grid-based simulations reveal that simulated HHG spectra can be quite sensitive to the CAP parameters,[53] which therefore need to be tested for this new choice of representation.

In the present work, we examine the extent to which the harmonic sequence can be simulated all the way through the cutoff value by combining Gaussian-orbital-based TDKS simulations with a CAP, which functions to absorb the leading portion of the outgoing wave packet that is generated by the strong laser pulse, preventing it from reflecting off of the edge of the finite basis and thereby creating an artificial interference pattern that can lead to spurious peaks in the high harmonic spectrum or else destroy the progression of harmonics altogether.

II. THEORY

A. High harmonic generation

The theoretical description of HHG, including the semiclassical three-step "recollision model," has been discussed and reviewed elsewhere.[2,12,15,23] This material is summarized briefly in order to place the TDKS simulations in context.

Consider a monochromatic laser pulse whose electric field is

$$\mathcal{E}(t) = \mathcal{E}_0 \cos(\omega_0 t), \tag{1}$$

and which is linearly polarized in the **z** direction. For an electron that is ejected at time $t = t_{\mathrm{ini}}$ with no initial velocity, setting $z(t_{\mathrm{ini}}) = 0 = \dot{z}(t_{\mathrm{ini}})$, one obtains[2]

$$z(t) = \frac{\mathcal{E}_0}{\omega_0^2}\left[\cos(\omega_0 t) - \cos(\omega_0 t_{\mathrm{ini}}) + (\omega_0 t_0 - \omega_0 t_{\mathrm{ini}})\sin(\omega_0 t_{\mathrm{ini}})\right]. \tag{2}$$

The kinetic energy of this electron is

$$E_{\mathrm{KE}} = 2U_{\mathrm{p}}\left[\sin(\omega_0 t) - \sin(\omega_0 t_{\mathrm{ini}})\right]^2, \tag{3}$$

where

$$U_{\mathrm{p}} = \frac{e^2\mathcal{E}_0^2}{4\,m\omega_0^2} = \frac{e^2 I}{2\epsilon_0 c m \omega_0^2} \tag{4}$$

is the ponderomotive energy for laser intensity $I = c\epsilon_0\mathcal{E}_0^2/2$,[12] defined as the time-averaged kinetic energy for the electron in the oscillatory laser field. A convenient formula is

$$U_p/\mathrm{eV} = 9.337 \times 10^{-14} \left(\frac{I}{\mathrm{W\ cm^2}}\right)\left(\frac{\lambda}{\mu\mathrm{m}}\right)^2, \tag{5}$$

where λ and I are the wavelength and intensity of the driving field, respectively.[2] The electron recombines with its source at time t_{rec} when $z(t_{\mathrm{rec}}) = 0$. The energy of the emitted photon created by the recombination event is

$$h\nu = E_{\mathrm{KE}}(t_{\mathrm{rec}}) + \mathrm{IE}, \tag{6}$$

where "IE" is the ionization energy of the molecule. The maximum photon energy (cutoff energy $\hbar\omega_{\mathrm{cutoff}}$) is determined using the maximum kinetic energy in Eq. (3) under the constraint that $z(t_{\mathrm{rec}}) = 0$ in Eq. (2). This results in an empirical cutoff law,

$$\hbar\omega_{\mathrm{cutoff}} = c_1 U_p + c_2 \mathrm{IE}, \tag{7}$$

where c_1 and c_2 are constants. The values[87] $c_1 = 3$ and $c_2 = 1$ are widely quoted,[12] although others have suggested $c_1 = 3.17$ and $c_2 = 1$,[88] $c_1 = 3.17$ and $c_2 = 1.32$,[68] or else $c_1 = 3.34$ and $c_2 = 1.83$.[89] However, harmonic progressions obtained from TDKS simulations may extend beyond this semiclassical cutoff law,[36] even for H_2^+ at the TDHF level where there are no electron correlation effects.[55]

Defining a phase $\theta = \omega_0 t$, with an initial $(t = t_{\mathrm{ini}})$ value θ_{ini} and a recombination $(t = t_{\mathrm{rec}})$ value θ_{rec}, the pair of values $\theta_{\mathrm{ini}} + n\pi$ and $\theta_{\mathrm{rec}} + n\pi$ also satisfy $z(\theta) = 0$ for integer values of n. Both the displacement z and velocity $\dot{z}$ change sign every half cycle, $z(\theta) = -z(\theta - \pi)$. As a result, the harmonic field $\mathcal{E}_{\mathrm{HHG}}(t)$ can be expressed as[2]

$$\begin{aligned}\mathcal{E}_{\mathrm{HHG}}(t) = \cdots + f(t + 2\pi/\omega_0) - f(t + \pi/\omega_0) + f(t) - f(t - \pi/\omega_0) \\ + f(t - 2\pi/\omega_0) - \cdots\end{aligned} \tag{8}$$

for some function $f(t)$. Following a Fourier transformation, Eq. (8) has nonzero values only at odd harmonic numbers. Within a semiclassical picture, the HHG spectrum of a molecule in a strong laser field thus consists of odd multiples of ω_0, up to the cutoff frequency, ω_{cutoff}.

B. TDKS simulations

A rigorous description of TDKS theory from first principles can be found in the work of Gross *et al.*,[24,25] and pedagogical treatments can be found in more recent reviews.[31,32] The adiabatic approximation (i.e., locality in time) is assumed throughout this work so that the time dependence of the exchange–correlation functional is carried strictly by the time-evolving density, $\rho(\mathbf{r}, t)$; ground-state functionals are therefore used without alteration. The time-dependent electron density is expressed in terms of time-dependent Kohn–Sham molecular orbitals (MOs),

$$\rho(\mathbf{r}, t) = \sum_k^{\mathrm{occ}} |\psi_k(\mathbf{r}, t)|^2. \tag{9}$$

Following a perturbation to the ground-state density, these MOs propagate in time according to the TDKS equation:

$$\mathrm{i}\hbar \frac{d\psi_k}{dt} = \hat{F}\psi_k(\mathbf{r}, t). \tag{10}$$

This is the one-electron analog of the time-dependent Schrödinger equation, and the Fock operator $\hat{F}$ functions as the effective Hamiltonian. The equation of motion for each ψ_k is numerically integrated to obtain time-evolving MOs $\psi_k(\mathbf{r}, t)$, starting from ground-state MOs at $t = 0$. The functions $\psi_k(\mathbf{r}, 0)$ are eigenfunctions of $\hat{F}$.

Equation (10) can be rewritten as an equivalent equation of motion for the density matrix $\mathbf{P}(t)$, which is the matrix representation of $\rho(\mathbf{r}, t)$ in some orthonormal basis. (This basis could simply be the Kohn–Sham MO basis.) Addition of a CAP makes $\hat{F}$ non-Hermitian, so the appropriate equation of motion for $\mathbf{P}(t)$ is

$$\mathrm{i}\hbar \frac{d\mathbf{P}}{dt} = \mathbf{FP} - \mathbf{PF}^\dagger. \tag{11}$$

Integration of Eq. (11) affords the time-dependent density matrix, $\mathbf{P}(t)$. We express the time propagation of the latter as

$$\mathbf{P}(t + \Delta t) = \mathbf{U}(t + \Delta t, t)\ \mathbf{P}(t)\ \mathbf{U}^\dagger(t + \Delta t, t), \tag{12}$$

where $\mathbf{U}(t + \Delta t, t)$ is a unitary time-propagation operator for the time step $t \to t + \Delta t$. Because both $\mathbf{P}$ and $\mathbf{F}$ in Eq. (11) are time-dependent quantities, the definition of $\mathbf{U}(t + \Delta t, t)$ involves time-ordering of the matrices $\mathbf{F}(t')$ at points t' along the integration $(t \le t' \le t + \Delta t)$,[90] or else a Magnus expansion of nested commutators.[33] Various forms for $\mathbf{U}(t + \Delta t, t)$ have been discussed in previous work,[33] including schemes that iterate the time propagation to self-consistency over the course of a single time step from t to $t + \Delta t$. In the present work, we use the modified-midpoint algorithm,[91] corresponding to a propagator

$$\mathbf{U}_N = \exp\left[-\mathrm{i}(\Delta t)\,\mathbf{F}_{N+1/2}\right] \tag{13}$$

that updates the density matrix from t_N to $t_{N+1} = t_N + \Delta t$. The quantity $\mathbf{F}_{N+1/2}$ is the Fock matrix at $t = t_N + \Delta t/2$.

For a molecule in a laser field, the Fock operator $\hat{F}$ consists of a field-free molecular part $(\hat{F}_0)$ augmented with an additional term $\boldsymbol{\mathcal{E}} \cdot \mathbf{r}$ involving the time-dependent electric field vector, $\boldsymbol{\mathcal{E}}(t)$. In addition, we add a CAP of the form $-\mathrm{i}W_{\mathrm{CAP}}(\mathbf{r})$, which is discussed in detail below. Both these additional terms added to $\hat{F}_0$ take the form of real-space potentials, and the total Fock operator including these additional terms is

$$\begin{aligned}\hat{F} &= \hat{F}_0 + \boldsymbol{\mathcal{E}}(t) \cdot \mathbf{r} - \mathrm{i}W^{\mathrm{CAP}}(\mathbf{r}) \\ &= \hat{F}' - \mathrm{i}W^{\mathrm{CAP}}(\mathbf{r}),\end{aligned} \tag{14}$$

where $\hat{F}' = \hat{F}_0 + \boldsymbol{\mathcal{E}}(t) \cdot \mathbf{r}$.

Our implementation of the CAP is similar to that used by Schlegel and co-workers to study strong-field ionization dynamics,[77–86] and which we have previously used to compute broadband x-ray absorption spectra.[34] The real-space function $W^{\mathrm{CAP}}(\mathbf{r})$ is constructed from a set of overlapping, atom-centered spherical potentials, each of which is zero within a cutoff radius

r_0 and then rises quadratically with curvature η. Explicitly, these functions are

$$f_k^{\mathrm{CAP}}(\mathbf{r}) = \begin{cases} 0, & \|\mathbf{r}-\mathbf{R}_k\| < r_0, \\ \eta(\|\mathbf{r}-\mathbf{R}_k\| - r_0)^2, & \|\mathbf{r}-\mathbf{R}_k\| \geq r_0 \end{cases} \tag{15}$$

for $k = 1, 2, \ldots, N_{\mathrm{A}}$, where $\mathbf{R}_k$ indicates the location of the kth nucleus and N_{A} is the number of atoms. The numerical value of $W^{\mathrm{CAP}}(\mathbf{r})$ is taken to be the minimum value of all the functions $f_k^{\mathrm{CAP}}(\mathbf{r})$, except that to avoid numerical problems, we impose a maximum value $E_{\max} = 10E_{\mathrm{h}}$ where E_{h} indicates the Hartree atomic unit of energy. The same tactic has been used in TDKS simulations of photoionization.[49,77,78] Schlegel and co-workers suggested setting r_0 at 3.5 times the atomic van der Waals radius, and they used $r_0 = 9.524\ a_0$ for hydrogen,[77,78] which is the value used in many of the calculations reported below although we also explore the use of larger and smaller values of r_0. The overall CAP function that appears in Eq. (14) is given by

$$W^{\mathrm{CAP}}(\mathbf{r}) = \min\{E_{\max}, f_1^{\mathrm{CAP}}(\mathbf{r}), \ldots, f_{N_{\mathrm{A}}}^{\mathrm{CAP}}(\mathbf{r})\}. \tag{16}$$

The matrix representation of W^{CAP} is required in order to propagate the Liouville–von Neumann equation. Introducing atom-centered Gaussian functions $\{g_\mu(\mathbf{r})\}$ for the atomic orbitals (AOs), this representation becomes

$$W_{\mu\nu}^{\mathrm{CAP}} = \int g_\mu(\mathbf{r})\, W^{\mathrm{CAP}}(\mathbf{r})\, g_\nu(\mathbf{r})\, d\mathbf{r}. \tag{17}$$

The integral is evaluated by numerical quadrature using the DFT quadrature grid.[92] The matrix $\mathbf{W}^{\mathrm{CAP}}$ does not depend on time and can be constructed once at the beginning of a TDKS simulation, and is then added to the Fock matrix $\mathbf{F}(t)$ at each time step. Note that $\mathbf{W}^{\mathrm{CAP}}$ is a symmetric matrix and therefore $-\mathrm{i}\mathbf{W}^{\mathrm{CAP}}$ in Eq. (14) is skew-Hermitian, meaning that $\mathbf{F}$ is not Hermitian despite the fact that $\mathbf{F}_0$ is real and symmetric at $t = 0$ when the CAP is turned off. Turning on the CAP abruptly at $t = 0$ spoils the stationarity of the ground state, but that property is destroyed anyway by the external field that is turned on at the same time.

For $t > 0$, $\mathbf{F} = -\mathbf{F}^\dagger$. This requires modification to the usual propagator, which is accomplished by approximate factorization of the relevant exponential:

$$\begin{aligned} e^{-\mathrm{i}(\Delta t)\mathbf{F}} &= \exp\left[-\mathrm{i}(\Delta t)(\mathbf{F}' - \mathrm{i}\mathbf{W}^{\mathrm{CAP}})\right] \\ &\approx \exp\left[-(\Delta t/2)\mathbf{W}^{\mathrm{CAP}}\right] \exp\left[-\mathrm{i}(\Delta t)\mathbf{F}'\right] \exp\left[-(\Delta t/2)\mathbf{W}^{\mathrm{CAP}}\right]. \end{aligned} \tag{18}$$

(This represents an application of the so-called split-operator technique.[90]) In this factorization, the leading and trailing exponentials involve symmetric matrices and the middle exponential involves a skew-Hermitian matrix. Each of these can be readily diagonalized to evaluate the necessary propagator, $\exp[-\mathrm{i}(\Delta t)\mathbf{F}]$.

It is worth noting the connection between the CAP and the heuristic lifetime model introduced by Klinkusch *et al.*[40] As noted by Coccia *et al.*,[69] adding an imaginary part to the self-consistent field (SCF) eigenvalues, $\varepsilon_p \to \varepsilon_p - \mathrm{i}\gamma_p$, formally corresponds to the use of the following CAP:

$$W^{\mathrm{CAP}}(\mathbf{r}) = \sum_p \gamma_p\, \psi_p^*(\mathbf{r})\, \psi_p(\mathbf{r}). \tag{19}$$

(The modification is made only to the unbound states, so $\gamma_p = 0$ unless $\varepsilon_p \geq 0$.) In practice, the use of the CAP defined by Eq. (19) is more complicated as compared to that in Eq. (17) because the former depends explicitly on the MOs. We will use Eq. (17) exclusively.

In our simulations, the external field $\boldsymbol{\mathcal{E}}(t) = \mathcal{E}(t)\mathbf{n}_{\mathrm{F}}$ is assumed to be linearly polarized in the direction of a unit vector $\mathbf{n}_{\mathrm{F}}$, with

$$\mathcal{E}(t) = \mathcal{E}_0 G(t) \sin(\omega_0 t) \tag{20}$$

where $\mathcal{E}_0$ and ω_0 are fixed parameters. We will explore both impulsive fields and continuous-wave fields, with $G(t) \equiv 1$ for the latter so that the field oscillates sinusoidally but does not decay. For the impulsive field, we use a Gaussian envelope function,

$$G(t) = \exp\left(-\frac{(t-t_{\mathrm{c}})^2}{2\sigma^2}\right). \tag{21}$$

These two fields are plotted in Fig. 1 for the same parameters $\mathcal{E}_0$ and ω_0.

The field is turned on at $t = 0$ where the MOs $\{\psi_k(\mathbf{r}, 0)\}$ represent the ground-state Kohn–Sham solution. Following sufficient time propagation, the HHG spectrum is computed from the Fourier transform ($\hat{\mathcal{F}}$) of the time-dependent dipole acceleration, $d_{\mathrm{A}}(t)$.[36,37] The dipole acceleration is the second derivative of the dipole moment, $\mu(t)$:

$$d_{\mathrm{A}}(t) = \frac{d^2\mu}{dt^2}. \tag{22}$$

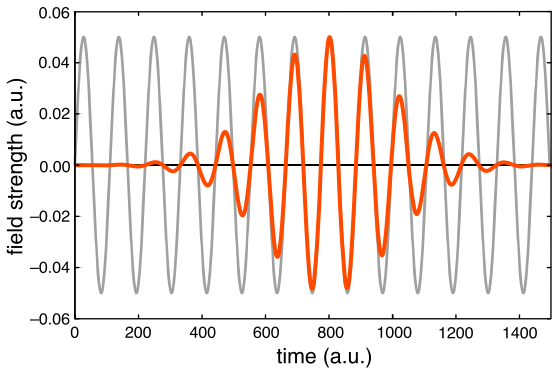

FIG. 1. An impulse field (in orange) and a continuous-wave field (in gray), as defined by $\mathcal{E}(t)$ in Eq. (20) with different functions $G(t)$. Parameters $\mathcal{E}_0 = 0.05$ a.u. and $\hbar\omega_0 = 1.55$ eV are used in both cases, corresponding to a laser intensity $I = 0.877 \times 10^{14}$ W/cm^2 at 800 nm. The continuous-wave field persists for the duration of the simulation while the impulse field is attenuated as shown, with parameters $t_{\mathrm{c}} = 800$ a.u. and $\sigma = 200$ a.u. characterizing the Gaussian envelope in Eq. (21).

The Fourier transform of this quantity is

$$d_A(\omega) = \frac{1}{t_{fin} - t_{ini}} \int_{t_{ini}}^{t_{fin}} d_A(t) e^{-i\omega t} dt. \quad (23)$$

Since the Fourier transform $[\hat{\mathcal{F}}: x(t) \mapsto X(\omega)]$ has the property

$$\hat{\mathcal{F}}\left[\frac{d^n}{dt^n} x(t)\right] = (i\omega)^n X(i\omega), \quad (24)$$

one may rewrite Eq. (23) as[37]

$$d_A(\omega) = \frac{-\omega^2}{t_{fin} - t_{ini}} \int_{t_{ini}}^{t_{fin}} \mu(t) e^{-i\omega t} dt. \quad (25)$$

This is the form of $d_A(\omega)$ that is used in practice; see Ref. 57 for some equivalent forms. The spectrum itself is equal to the dipole oscillator strength function,

$$S(\omega) \propto |d_A(\omega)|^2 \quad (26)$$

up to proportionality constants that are not important here.[12,37,54]

III. COMPUTATIONAL DETAILS

The results presented here are based on a completely new implementation[34] of the TDKS module in Q-Chem v. 5.4,[93] replacing the original TDKS code written by Nguyen *et al.*[94,95] In the new module, time propagation can be accomplished based on either the modified-midpoint algorithm,[91] which is used here, or else self-consistent predictor–corrector algorithms.[33]

A. TDKS simulations

Calculations are performed for H_2 at $R = 0.75$ Å and for H_2^+ at $R = 2.0\ a_0 = 1.058\,354$ Å using a spin-unrestricted formalism. The field is aligned along the internuclear axis, which we take to be polarization in the z direction, $\mathbf{n}_F = (0, 0, 1)$.

All simulations use the same carrier frequency for the external field, $\hbar\omega_0 = 1.55$ eV $\approx 0.0570 E_h$ corresponding to $\lambda = 800$ nm. All H_2 simulations are performed using a field amplitude $\mathcal{E}_0 = 0.05$ a.u. in Eq. (20), corresponding to $I = 0.877 \times 10^{14}$ W/cm^2. Conversion between $\mathcal{E}_0$ and I can be made either using Eq. (5) or else by noting that the atomic unit of electric field strength is[12,96]

$$\mathcal{E}_{a.u.} = \frac{e}{4\pi\epsilon_0 a_0^2} \approx 5.14 \times 10^9 \text{ V/cm}, \quad (27)$$

while that of laser intensity is[12]

$$I_{a.u.} = \frac{1}{2} c\epsilon_0 \mathcal{E}_{a.u.}^2 \approx 3.51 \times 10^{16} \text{ W/cm}^2. \quad (28)$$

In order to make contact with previous literature, some H_2^+ simulations are reported at field intensities including $I = 0.488 \times 10^{14}$, 1.95×10^{14}, and 2.92×10^{14} W/cm^2, again for $\lambda = 800$ nm. These values correspond to $\mathcal{E}_0 = 0.037\,3$, 0.0745, and 0.0913 a.u., respectively.

For the Gaussian-impulse field [Eq. (21)], we take $t_c = 800$ a.u. and $\sigma = 200$ a.u. and use a total simulation time of 1500 a.u. (≈36.3 fs), extending just beyond the support of the envelope function $\mathcal{E}(t)$ for this set of parameters. We also report simulations using a continuous-wave field where the total simulation time is 5000 a.u. (≈121 fs). These simulations use the same values $\mathcal{E}_0$ and ω_0 that define the impulsive field so that the peak value of $\mathcal{E}(t)$ is the same in both cases. (Both fields are plotted in Fig. 1.) At low field intensities, vibrational motion may destroy coherences needed to obtain the highest harmonic orders,[59] but those effects are not considered here.

The shape of the CAP is described using Eq. (15) with various values of the turn-on radius, $r_0 = 4.0$–$18.5\ a_0$. The curvature parameter is tested within a range $\eta = 0.4$–$4.0\ E_h/a_0^2$. The time propagation algorithm is described in Sec. II B, and the time step is $\Delta t = 0.1$ a.u.. While performing the Fourier transform that is indicated in Eq. (25), a Hann window function

$$w(t) = \sin^2\left(\frac{\pi t}{t_{fin} - t_{ini}}\right) \quad (29)$$

is applied to the time series of $\mu(t)$ data. Although Eq. (25) formally corresponds to a three-dimensional Fourier transform, in practice we find that the Fourier transform of the z-component $\mu_z(t)$ provides a HHG spectrum in good agreement with the full transform; see Fig. S1 for a comparison. Since the perturbing field is polarized in the z direction, the $\mu_z(t)$ data may be less affected by numerical noise and therefore only $\mu_z(t)$ is used to compute the spectra shown below.

B. SCF methods

Since HHG involves ionization and electron recombination, the asymptotic behavior of the exchange–correlation function is crucial.[36,37,39] We use a LRC variant of a range-separated hybrid functional, specifically the LRC-ωPBE functional[46] with range-separation parameter $\omega = 0.3\ a_0^{-1}$. LRC functionals, as a subset of range-separated hybrid functionals,[48] are characterized by an asymptotic exchange functional that becomes 100% Hartree–Fock (HF) exchange for $r_{12} \gg 1/\omega$. This ensures that the asymptotic behavior of the exchange potential is $-1/r$. Not all range-separated hybrid functionals enforce correct asymptotic behavior; see Ref. 48 for a discussion. To assess the role of electron correlation, we will also carry out some simulations at the level of TDHF theory, meaning that the functional consists of HF exchange only with no correlation and no range separation.

The initial ground-state SCF calculation is converged using a threshold of $10^{-9}\ E_h$ for the maximum value of $[\mathbf{F}, \mathbf{P}]$. A numerical threshold of $\tau = 10^{-12}$ a.u. is used for shell-pair formation and integral screening in all Fock builds. The SG-1 quadrature grid[98] is used for the exchange–correlation functional integration. Because its radial quadrature is designed for the interval $r \in [0, \infty)$, this grid has been found to be adequate even in the presence of extremely diffuse basis functions,[99] at least for GGA functionals and hybrids thereof. Meta-GGAs and some other recently developed functionals require denser grids,[92] but such functionals are not considered in the present work.

C. Basis sets

In previous simulations of HHG using Gaussian basis functions, Luppi and co-workers[41,55–58] used a sequence of extremely diffuse basis sets that they call *n*-aug-cc-pV*X*Z. These start from the standard aug-cc-pV*X*Z basis sets,[97] corresponding to $n = 1$, and then add uncontracted diffuse functions with angular momenta $\ell = 0, 1$, and 2 for each subsequent value of n. The construction of such basis sets was described in Ref. 97, where they were called *x*-aug-cc-pVXZ with x = d, t, or q, corresponding to $n = 2$, 3, or 4 in the present notation. Diffuse exponents for hydrogen in the *n*-aug-cc-pVTZ sequence of basis sets are provided in Table I for $n \leq 6$. Scaling factors for the diffuse exponents are ≈4 (depending on the value of ℓ), as in the original basis sets reported by Woon and Dunning.[97] These scaling factors (as opposed to something smaller) help to avoid numerical linear dependencies in polyatomic molecules. The same observation has been made regarding the highly diffuse basis sets used to describe weakly bound anions.[71,99]

We use *n*-aug-cc-pVTZ (hereafter abbreviated *n*-aTZ) because Coccia *et al.* observed that HHG spectra change little for X = Q or 5, relative to X = T.[57] Other studies have also confirmed that the diffuse functions are much more important for HHG than the choice of valence functions.[55] For a laser intensity $I = 10^{14}$ W/cm^2, HHG spectra obtained using either 5-aTZ or 6-aTZ are essentially identical; see Fig. S2. This indicates that TDKS/5-aTZ spectra are converged with respect to the number of diffuse shells.

Long ago, Kaufmann *et al.*[100] described a set of diffuse basis functions intended to represent Rydberg and continuum states, which have recently been used to compute high harmonic spectra in atom-centered Gaussian basis sets.[57–59] Exponents for Kaufmann's sequence with $n \leq 8$, and with angular momenta $\ell = 0, 1$, and 2, can be found in Ref. 57, and this has been called the "8K" set of functions. A smaller "5K" set ($n \leq 5$ and $\ell \leq 2$) has also been described.[55] Both sets have been used in recent simulations of HHG spectra using Gaussian basis functions.[55,57–59] It is worth noting that even the larger 8K set is considerably less diffuse as compared to 5-aTZ. The smallest exponent in the 8K set is $\zeta = 9.615 \times 10^{-3}\ a_0^{-2}$ for $\ell = 0$, which is 104× larger (more compact) than the most diffuse exponent in 5-aTZ. For the $\ell = 1$ and $\ell = 2$ functions, the 8K exponents are more than 30× larger than the smallest p and d exponents in 5-aTZ. With respect to the continuum states, the 5-aTZ basis may therefore be considered to afford the superior description.

It is possible that these Kaufmann *n*K functions may afford a better description of angular momentum components as compared to standard even-tempered diffuse functions. We therefore tested the 6-aTZ+5K basis set for H_2^+ at several different field intensities, with HHG spectra that are plotted in Fig. S3. For field intensities $I \lesssim 2 \times 10^{14}$ W/cm^2, we find very little difference as compared to 5-aTZ, the latter of which contains 60 fewer basis functions per hydrogen atom. Even for $I = 3 \times 10^{14}$ W/cm^2, which is 3× larger than the laser intensity used for most of the calculations reported below, only minor differences are observed between the 6-aTZ+5K and 5-aTZ results. As such, the 5-aTZ basis set is used for all subsequent calculations reported here.

Finally, we note that the 5-aTZ basis set is also more diffuse than those that have been used to simulate strong-field ionization dynamics with CAPs. The smallest exponents used in some recent studies are $\zeta = 3.2 \times 10^{-3}\ a_0^{-2}$,[84–86] while even less diffuse basis sets have been used in other work.[77–82] Although diffuse functions with $\ell = 3$ have been used where the angular details of the photoionization cross sections were of interest,[80–85] convergence studies of HHG spectra suggest that these are unnecessary in the present context,[41] and no diffuse $\ell = 3$ functions are used in the *n*-aTZ basis sets.

Gaussian exponents ζ from Table I are converted into radial half-widths at half-maximum (HWHM) in Table II using the formula[71]

$$\mathrm{HWHM}(\zeta) = \frac{\sqrt{\ln 2}}{\zeta^{1/2}} \approx 0.8326\,\zeta^{-1/2}. \tag{30}$$

For 5-aTZ, the smallest exponent affords $\mathrm{HWHM}(\zeta) \approx 87\ a_0$, which can lead to numerical linear dependency problems if thresholds are set too loose. We find that an integral screening threshold $\tau = 10^{-12}$ a.u. is adequate for 5-aTZ, as judged by comparison to calculations using $\tau = 10^{-16}$ a.u., the latter of which corresponds to machine precision in double-precision arithmetic. (See Fig. S2 for the numerical comparisons.) The value $\tau = 10^{-12}$ a.u. is therefore used for all simulations reported below. For the 6-aTZ basis set, which is part of the 6-aTZ+5K basis used in convergence tests reported above, we find that $\tau = 10^{-12}$ a.u. is not sufficient to yield numerically stable simulations. In that case, we use $\tau = 10^{-16}$ a.u..

D. Other convergence tests

Convergence with respect to the basis set (Figs. S2 and S3) and numerical thresholds (Fig. S3) was addressed above.

TABLE I. Gaussian exponents, ζ (in a_0^{-2}), for hydrogen in the multiply-augmented *n*-aTZ basis sets.

			n-aug-cc-pVTZ				
	cc-pVTZ[a]	aug-cc-pVTZ	$n = 2$[b]	$n = 3$	$n = 4$	$n = 5$	$n = 6$
s	1.027×10^{-1}	2.526×10^{-2}	6.210×10^{-3}	1.527×10^{-3}	3.753×10^{-4}	9.227×10^{-5}	2.268×10^{-5}
p	3.880×10^{-1}	10.200×10^{-2}	26.800×10^{-3}	7.042×10^{-3}	18.501×10^{-4}	48.612×10^{-5}	12.773×10^{-5}
d	10.570×10^{-1}	24.700×10^{-2}	57.700×10^{-3}	13.479×10^{-3}	31.487×10^{-4}	73.555×10^{-5}	17.183×10^{-5}

[a]Smallest exponent in the parent basis set.
[b]Also known as d-aug-cc-pVTZ.[97]

TABLE II. Gaussian half-widths at half-maximum (HWHM, in bohr) for the most diffuse *n*-aTZ basis function on hydrogen.

		n-aug-cc-pVTZ				
	cc-pVTZ	$n = 1$[a]	$n = 2$[b]	$n = 3$	$n = 4$	$n = 5$
s	2.60	5.24	10.57	21.31	42.98	86.68
p	1.34	2.61	5.09	9.92	19.36	37.76
d	0.81	1.68	3.47	7.17	14.84	30.70

[a]Conventional aug-cc-pVTZ basis set.
[b]Also known as d-aug-cc-pVTZ.[97]

Convergence with respect to grid-based TDKS simulations is discussed in Sec. IV B, as a proper comparison in that case requires the introduction of a CAP to match the absorbing boundary conditions in the grid-based simulation.

To test for convergence with respect to the finite time step Δt that is used to integrate the TDKS equation, we performed simulations using values ranging from $\Delta t = 0.01$ a.u. ($= 2.42 \times 10^{-19}$ s) to $\Delta t = 0.20$ a.u., corresponding to Nyquist frequencies ranging from 8.5 keV to 427 eV, respectively.[33,34] These simulations use the impulse field that is plotted in Fig. 1. Since the external field is applied in the z direction, coinciding with the axis of the molecule, we can use $\mu_z(t)$ to assess the impact of Δt. From the $\mu_z(t)$ data in Fig. 2, it is evident that the time-dependent dipole moments computed using different values of Δt track one another quite well. Taking the smallest time step ($\Delta t = 0.01$ a.u.) as the benchmark, differences in μ_z for the larger values of Δt are on the order of 10^{-4} a.u. in a total dipole moment whose magnitude ranges to almost 0.4 a.u. When the time step is increased to $\Delta t = 0.2$ a.u., the deviations in μ_z increase in magnitude to $\sim 10^{-2}$ a.u. and some spurious high-frequency oscillations appear (Fig. 3). As such, $\Delta t = 0.1$ a.u. is the best choice for accuracy and efficiency and is used for all subsequent simulations.

Time steps of either $\Delta t = 0.05$ a.u.[55] or else $\Delta t = 0.1$ a.u.[57] have been used in previous simulations of HHG using Gaussian basis functions. Figure S4 demonstrates that HHG spectra computed with $\Delta t = 0.10$ a.u. are converged with respect to those computed using $\Delta t = 0.01$ a.u.. The properties of the Fourier transform result in sharpening of the peaks (relative to background noise) as the time step is decreased, but the fine details of the peaks are unchanged for time steps as large as $\Delta t = 0.10$ a.u.. This is true despite the fact that the spectra in Fig. S4, which are computed in the absence of a CAP, are rather noisy. Even this noise is faithfully reproduced using $\Delta t = 0.10$ a.u..

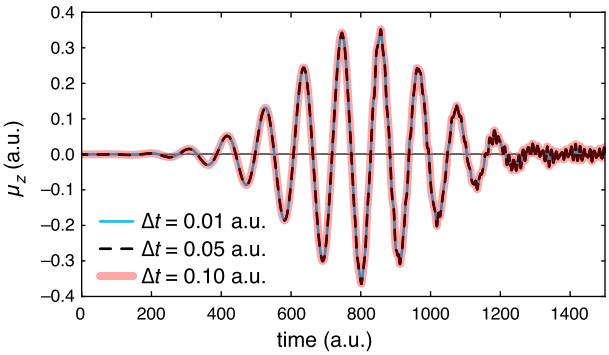

FIG. 2. Time-dependent dipole moment $\mu_z(t)$ for the H_2 molecule, obtained from TDKS simulations at the LRC-ωPBE/5-aTZ level using various time steps, Δt. The simulations use the impulse field shown in Fig. 1.

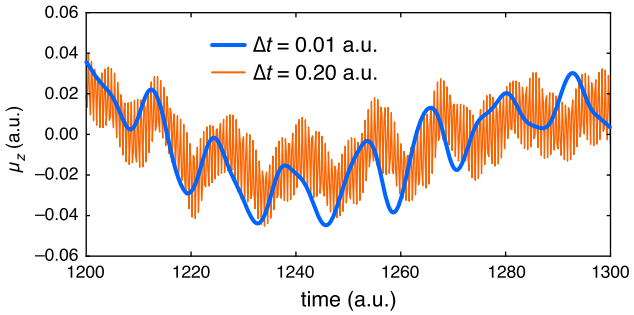

FIG. 3. Time-dependent dipole moment $\mu_z(t)$ for H_2, obtained from TDKS simulations at the LRC-ωPBE/5-aTZ level with two different time steps. The simulations use the impulse field shown in Fig. 1, corresponding to $I = 0.877 \times 10^{14}$ W/cm^2. Data for $\Delta t = 0.01$ a.u. are the same as those plotted in Fig. 2. For clarity, only a portion of the simulation is shown, but these simulations have the same $t = 0$ starting point as those in Fig. 2.

IV. RESULTS AND DISCUSSION

A. Control experiments

Figure 4 presents HHG spectra for H_2 computed using TDKS simulations with either the HF or the LRC-ωPBE functional. In these numerical experiments, no CAP is applied and the laser field is the same impulse field that was used for the stability tests, with a total time propagation of 1500 a.u.. Neither spectrum in Fig. 4 conveys much of the known characteristics of a high harmonic spectrum, in concurrence with previous TD-CIS simulations when no correction for the unbound states is applied.[41] Only the first two or three harmonics are well resolved, and differences between the TDHF and TDKS results are minor in comparison to the broader observation that no well-resolved harmonic progression is obtained in either case.

For $I = 0.877 \times 10^{14}$ W/cm^2 and $\lambda = 800$ nm, Eq. (5) affords $U_p = 5.38$ eV. At the HF/5-aTZ level, the IE is either 15.3 eV (ΔSCF value) or 16.1 eV (Koopmans value, corresponding to $-\varepsilon_{HOMO}$), and at the LRC-ωPBE/5-aTZ level it is either 16.3 eV (ΔSCF) or 14.3 eV (Koopmans). Using the most recent estimate of the cutoff energy,[89] corresponding to Eq. (7) with $c_1 = 3.34$ and $c_2 = 1.83$, one thus obtains $\hbar\omega_{cutoff} = 44.1$–$47.8$ eV, corresponding to 28–30 harmonics for $\hbar\omega_0 = 1.55$ eV. Although normally one would consider the ΔSCF value to be the superior DFT estimate of the IE, as compared to the Koopmans value, the latter may be more appropriate in the context of a TDKS simulation because excitations into unbound MOs afford ionization channels. Taking IE $= -\varepsilon_{HOMO}$, the cutoff is estimated as the 30th harmonic for the HF simulation and the 28th harmonic for LRC-ωPBE. As indicated in Fig. 4, the simulated signals drop by several orders of magnitude precisely in this energy range.

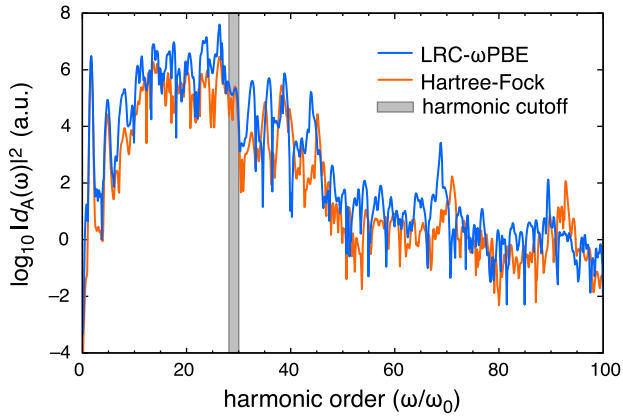

FIG. 4. HHG spectra for H_2 computed from TDKS/5-aTZ simulations with two different functionals and no CAP. An impulsive field is applied, with parameters corresponding to $I = 0.877 \times 10^{14}$ W/cm^2 (Fig. 1), and the simulations were propagated in time for 1500 a.u.. The vertical axis shows the signal $|d_A(\omega)|^2$ on a logarithmic scale, and the horizontal axis is measured in multiples of the field frequency, $\hbar\omega_0 = 1.55$ eV (corresponding to $\lambda = 800$ nm). Harmonic cutoffs estimated from Eq. (7) are indicated (see text).

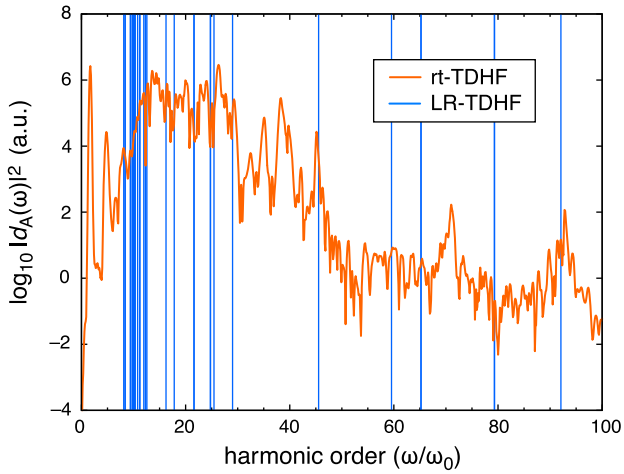

FIG. 5. HHG spectrum of H_2 (in orange, corresponding to the TDHF/5-aTZ data from Fig. 4) overlaid with vertical excitation energies computed from a LR-TDHF calculation (in blue). Only LR-TDHF transitions with oscillator strengths above 10^{-10} are included.

Notably, however, the intensity persists to significantly higher harmonic orders, albeit much attenuated, and a harmonic progression persists as well. This progression is somewhat resolved up to the 45th harmonic, with additional features around $\omega/\omega_0 = 68$–70 and 90–92, depending on which functional is used. We hypothesize that this behavior results from artificial confinement of the electron due to the finite extent of the Gaussian basis set. Higher-energy parts of the outgoing wave that should be ionized are instead confined and reflected, generating spurious interference features and generally contributing to a noisy spectrum.

To investigate this hypothesis, Fig. 5 overlays the HHG spectrum computed at the TDHF level with an excitation spectrum computed using linear response (LR) TDDFT. (For clarity, only the LR-TDHF states with oscillator strengths greater than 10^{-10} are shown, as these should dominate the transition rate.) Resonances with LR-TDDFT excited states do explain some of the peaks above the harmonic cutoff, in particular the peaks around the 45th and 92nd harmonics in the TDHF spectrum of Fig. 4. These resonances lie well above the ionization threshold of the molecule and can thus be considered artifacts of the finite Gaussian basis set that prevents the molecule from ionizing. The LR-TDDFT calculation also exhibits resonances coinciding already with the 8th, 9th, and 10th harmonics, and these features may be at least partially responsible for the lack of resolution that is observed in the real-time simulations, even at lower harmonic orders. The LR-TDDFT excitation energies do not explain the other above-cutoff features, however, such as those appearing around the 38th and 72nd harmonics (see Fig. 5), although it is worth emphasizing that the intensity scale in Fig. 4 is logarithmic and features above the 45th harmonic are attenuated by $10^5\times$ or more as compared to the most intense pre-cutoff features. In an effort to reduce or exclude these artifacts, we next turn to TDKS simulations using a CAP.

B. Evaluation of CAP parameters

Figure 6 presents a side-by-side comparison of the HHG spectra computed with and without a CAP. The CAP has little effect on the first few harmonics, but beyond the 10th harmonic the noise in the original spectrum (computed without the CAP) is greatly reduced and consequently distinct peaks emerge at odd harmonic orders, as anticipated. Spectra computed with the CAP, using either the HF or LRC-ωPBE functional, are compared side-by-side in Fig. 7. Above the 30th harmonic, the LRC-ωPBE spectrum continues to exhibit markedly larger intensity as compared to the HF spectrum although a steep drop-off is evident in either case around the cutoff frequency predicted using Eq. (7). Above the 60th harmonic there is some slight resurgence in intensity, but by that point the intensity has fallen by more than ten decades relative to the early harmonics and it is unclear whether the signal is distinguishable from noise.

We next explore variations in the CAP parameters r_0 and η that are defined in Eq. (15). We do this first for H_2^+, for which the TDHF method is exact up to numerical convergence that was examined above. For this system, grid-based simulations of HHG spectra are available,[55] which allows us to test the Gaussian orbital representation and the choice of boundary conditions. Figure 8 compares HHG spectra computed at the TDHF/5-aTZ level with a CAP (using our code) to results obtained in Ref. 55 using a real-space grid with absorbing boundary conditions. Spectra computed from a Gaussian-based TDHF/6-aTZ+5K simulation with a heuristic lifetime model are also shown, from Ref. 55.

The present simulations employ two different sets of CAP parameters for H_2^+, namely, $r_0 = 9.524\ a_0$ and $\eta = 4.0\ E_h/a_0^2$ in Figs. 8(a)–8(c), vs $r_0 = 18.5\ a_0$ and $\eta = 0.1\ E_h/a_0^2$ in Figs. 8(d)–8(f). (Spectra for both sets of CAP parameters are plotted on the same axes in Fig. S5, without the data from Ref. 55.) Unlike the simulations reported above, which used an impulsive field and were propagated for 1500 a.u. in time, the simulations in Fig. 8 used a

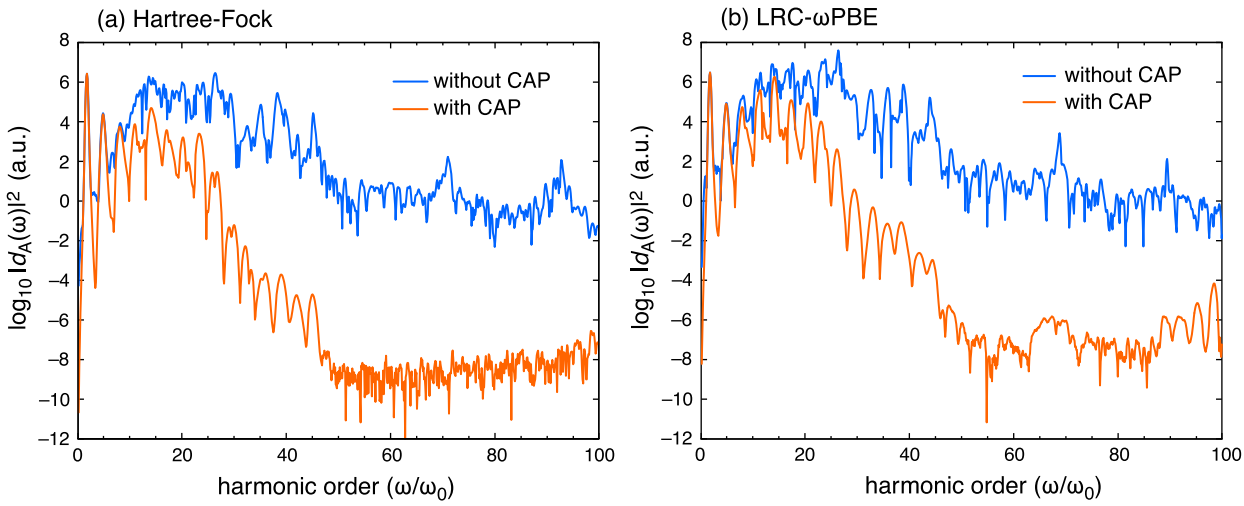

FIG. 6. Comparison of HHG spectra for H_2 computed from simulations with and without a CAP, using (a) TDHF theory and (b) TDKS with the LRC-ωPBE functional, using the 5-aTZ basis set in either case. The field is an impulse (Fig. 1), and all simulations are propagated for 1500 a.u. in time. (Spectra computed without the CAP are the same as those in Fig. 4.) CAP parameters are set to $r_0 = 9.524\ a_0$ and $\eta = 4.0\ E_h/a_0^2$. The vertical scale is logarithmic, and the horizontal axis is in units of the fundamental frequency, $\omega_0 = 1.55$ eV.

continuous-wave field and were propagated for 5000 a.u., but only the final 1000 a.u. of simulation data were used to compute the spectrum. The continuous waveform provides better resolution of the harmonics, but only if a CAP is employed; see Fig. S6 for an example of a continuous-wave spectrum without a CAP. The latter is so noisy that the cutoff energy is only barely evident above the noise.

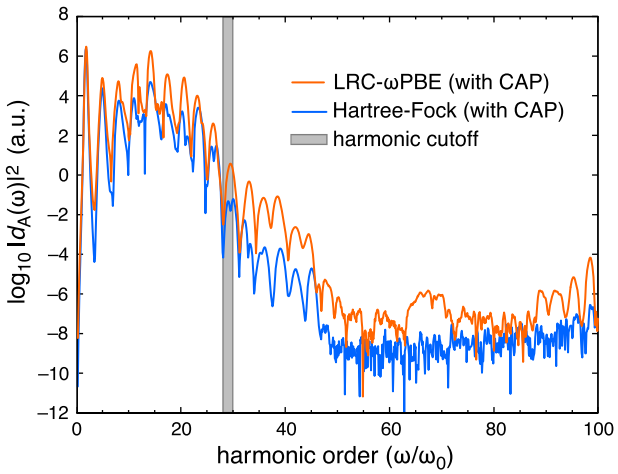

FIG. 7. Comparison of HHG spectra for H_2 computed from TDKS and TDHF simulations with a CAP. The field is impulsive, corresponding to $I = 0.877 \times 10^{14}$ W/cm^2 (see Fig. 1), and all simulations are propagated for 1500 a.u. in time. These are the same spectra that are plotted in Fig. 6, omitting results obtained without the CAP. The CAP parameters are set to $r_0 = 9.524\ a_0$ and $\eta = 4.0\ E_h/a_0^2$. The harmonic cutoff estimated from Eq. (7) is indicated.

Although there are some clear differences between grid-based HHG spectra and results obtained from the present implementation, especially in the relative intensities of the first few harmonics and in the length of the harmonic progression that is obtained, the onset of strong attenuation of the harmonic sequence is roughly similar in the present work and in the grid-based simulations from Ref. 55. The larger and softer CAP ($r_0 = 18.5\ a_0$ and $\eta = 0.1\ E_h/a_0^2$) does a much better job of matching full harmonic progression obtained in grid-based simulations, which extends well beyond the cutoff predicted using the semiclassical formula in Eq. (7). The smaller, stronger CAP ($r_0 = 9.524\ a_0$ and $\eta = 4.0\ E_h/a_0^2$) attenuates the harmonic progression too quickly.

Convergence tests reported in Fig. S3 indicate that TDHF/5-aTZ simulations are converged with respect to the 6-aTZ+5K basis, therefore any differences between the two sets of Gaussian orbital-based simulations in Fig. 8 are attributable to the heuristic lifetime model vs the CAP. For the strongest field intensity ($I = 3 \times 10^{14}$ W/cm^2), the CAP-based simulations reported here are in much better agreement with the grid-based spectra as compared to results obtained using a heuristic lifetime model.

Although grid-based simulations are often taken as benchmarks for real-time electron dynamics, it is worth noting that even these simulations require absorbing boundary conditions and are therefore not free of arbitrary parameters. HHG spectra are sensitive to these parameters, even in a grid representation.[53] Comparison to results from smooth exterior complex scaling,[101] which is a CAP-free alternative to absorbing boundary conditions, suggests that even grid-based simulations with a CAP suffer from significant numerical noise above the harmonic cutoff, as the CAP does not completely quench the reflected wave.[53] We therefore find it encouraging that simulations with parameters $r_0 = 18.5\ a_0$ and $\eta = 0.1\ E_h/a_0^2$ do a reasonable job of reproducing the grid-based results, which were performed with an absorbing potential at 50 a_0 away from the

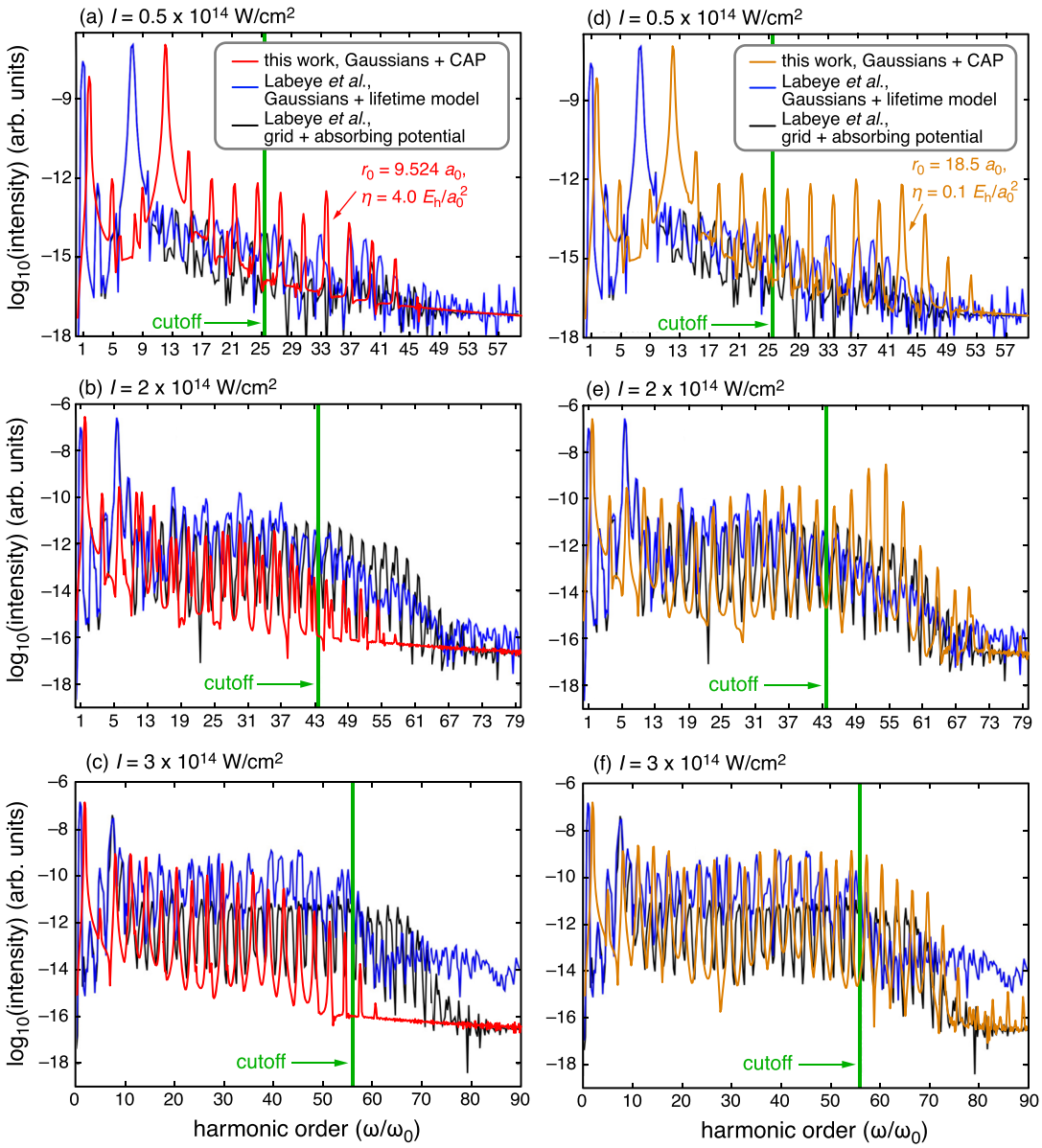

FIG. 8. HHG spectra for H_2^+ computed using $\hbar\omega_0 = 1.55$ eV and $\lambda = 800$ nm for three different laser intensities, as indicated. Results from the present work (TDHF/5-aTZ level, in red and orange) are based on continuous-wave simulations using CAP parameters $r_0 = 9.524\ a_0$ and $\eta = 4.0\ E_h/a_0^2$ (a–c) or $r_0 = 18.5\ a_0$ and $\eta = 0.1\ E_h/a_0^2$ (d–f). All simulations were propagated for 5000 a.u. of time using $\Delta t = 0.1$ a.u., but only the final 1000 a.u. was used to compute the spectrum. Spectra were then scaled to match the maximum intensity and the baseline of the grid-based TDKS simulations reported by Labeye *et al.*[55] (in black). The results in blue were reported in Ref. 55 at the TDHF/6-aTZ+5K level using a heuristic lifetime model rather than a CAP. Semiclassical harmonic cutoffs (green vertical lines) were estimated using Eq. (7).[55] Data from the study by Labeye *et al.* are reproduced with permission from Labeye *et al.*, "Optimal basis set for electron dynamics in strong laser fields: The case of molecular ion H_2^+," J. Chem. Theory Comput. **14**, 5846–5858 (2018). Copyright 2018 American Chemical Society.

molecular ion.[55] It is possible that tuning the CAP parameters used herein might afford better agreement with the grid-based simulations, but we have not pursued this.

Returning to H_2, Fig. 9 shows HHG spectra computed at the HF/5-aTZ level using four sets of CAP parameters. The parameters $r_0 = 9.524\ a_0$ and $\eta = 4.0\ E_h/a_0^2$ that are used in Fig. 9(a) are the same as those used in the impulse-field simulations described above (Fig. 7); comparison of the two spectra demonstrates how the continuous waveform affords a much better resolved set of peaks, up to and beyond the harmonic cutoff from Eq. (7). We attribute

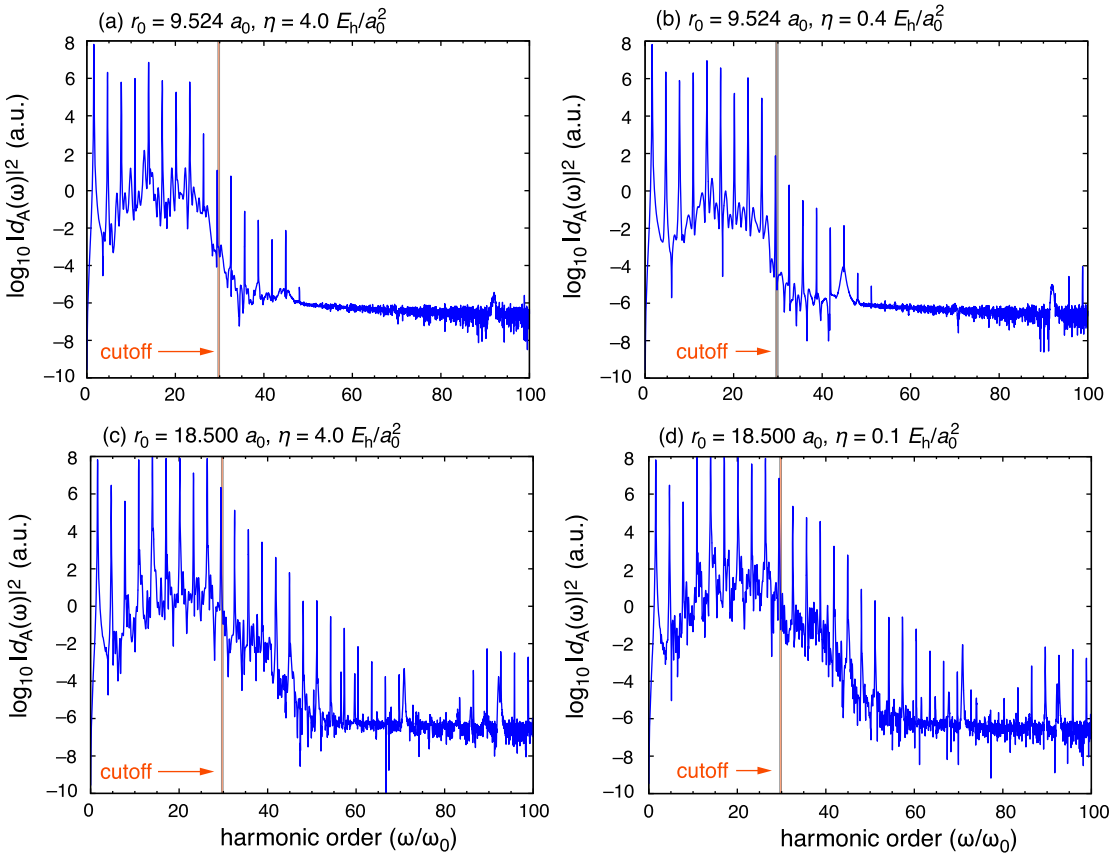

FIG. 9. (a)–(d) Comparison of HHG spectra for H_2 computed at the TDHF/5-aTZ level using various values of the parameters r_0 and η that define the CAP, as indicated. All four simulations were propagated for 5000 a.u. of time in the presence of a continuous-wave field corresponding to $I = 0.877 \times 10^{14}$ W/cm^2 (Fig. 1). The semiclassical harmonic cutoff [Eq. (7)] is indicated.

this superior resolution to the fact that the system experiences more cycles of the laser field as compared to the impulsive simulation.

As compared to the spectrum in Fig. 9(a), the one reported in Fig. 9(b) uses the same turn-on radius (r_0) but reduces the curvature (η) by a factor of ten. This change has a negligible effect on the pre-cutoff features and only a minor effect on the six sharp peaks that appear just above the cutoff. The feature around the 92nd harmonic, which we previously attributed to an above-threshold resonance, becomes more pronounced but the intensity is so low that this feature is clearly separated from the HHG spectrum.

To compute the spectra shown in Figs. 9(c) and 9(d) we used a much larger turn-on radius, $r_0 = 18.5\ a_0$, with two different values of η. The resulting harmonic progressions do not drop nearly so precipitously at the 30th (cutoff) harmonic as they did for the smaller value of r_0, and sharp (but gradually attenuated) features are observed out to at least at the 72nd harmonic where they vanish into the background but reappear at somewhat higher energies. Notably, the CAP parameters in Fig. 9(d) are the ones that afforded good agreement with grid-based TDKS simulations for H_2^+ (Fig. 8). Therefore it is clear that the smaller CAP radius of $r_0 = 9.524\ a_0$ prematurely attenuates the harmonic progression. For $r_0 = 18.5\ a_0$, the difference between the two choices of η in Fig. 9 is that the larger value [$\eta = 4.0\ E_h/a_0^2$, Fig. 9(c)] provides a clearer indication of where the harmonic sequences vanish into baseline noise, around the 72nd or 74th harmonic. Higher-energy parts of the spectrum should not be taken seriously.

Figure S7 plots the HHG spectrum obtained using $r_0 = 4.0\ a_0$ and $\eta = 4.0\ E_h/a_0^2$. In this case, the much smaller value of r_0 destroys the entire harmonic progression, even at pre-cutoff energies, as nearly all of the harmonics are swallowed by the absorbing potential. In fact, these harmonics are dissolved by the small-r_0 CAP because the electron density itself is annihilated over the course of the simulation if the CAP is set too close to the molecule. This is illustrated in Fig. 10(a), which plots the ionization rate (time-dependent value of the integrated number of electrons) for a simulation with $r_0 = 4.0\ a_0$. The corresponding HHG spectrum (Fig. S7) fails to evince any clear harmonics beyond the first three, and two of those are severely attenuated.

Ionization rates for other sets of CAP parameters, with $r_0 \geq 9.524\ a_0$ in each case, are plotted in Fig. 10(b). For these simulations, the ionization rate is much slower and $\lesssim 0.02e$ is lost over

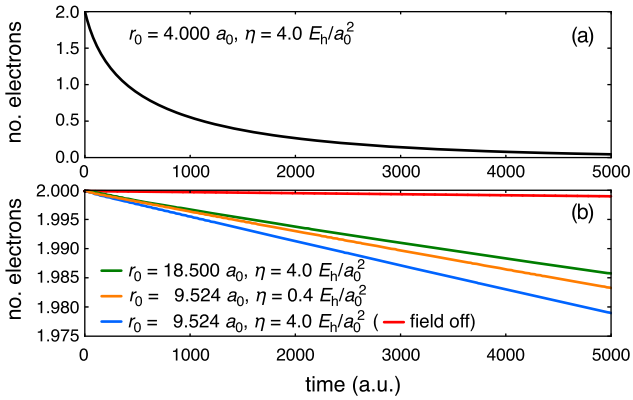

FIG. 10. Ionization rates for continuous-wave simulations at the TDHF/5-aTZ level using (a) a small value of r_0 that annihilates the entire electron density over the course of 5000 a.u. of time propagation, vs (b) CAP parameter sets (r_0, η) leading to much slower ionization. The "field off" result in (b) illustrates the electron loss in the absence of any perturbing field, which is due to the CAP itself. The CAP parameters for this "field off" simulation are r_0 = 9.524 a_0 and η = 4.0 E_h/a_0^2.

5000 a.u. of time propagation. As noted elsewhere,[50] introduction of a CAP at $t = 0$ creates a non-stationary state that induces electron loss even in the absence of an external perturbing field, but for CAP parameters r_0 = 9.524 a_0 and η = 4.0 E_h/a_0^2, these losses amount to <0.01e over 5000 a.u. of time propagation. Furthermore, ionization rates obtained using r_0 = 9.524 a_0 are not so different from what is obtained with r_0 = 18.5 a_0 that it might lead one to suspect that the smaller CAP attenuates so much of the harmonic progression as it does. Thus, the ionization rate proves not to be a very stringent diagnostic for the quality of the HHG spectrum.

The conclusion from these variations in the CAP parameters is that the CAP plays a critical role in obtaining characteristic HHG spectra, as without it the spectra are overwhelmed by noise and higher harmonics are missing. The 1% of the electron density that is annihilated by the slow-ionization simulations [Fig. 10(b)] is critical to obtaining a clean HHG spectrum, as otherwise this part of the density becomes a reflected wave whose interference with the outgoing wave leads to noise. On the other hand, if the turn-on radius of the CAP is set too close to the nuclei (small r_0), then the electron density is absorbed too quickly and the system does not experience enough field cycles to generate well-resolved harmonics (Fig. S7).

It is interesting to consider these observations about electron loss within the context of the semiclassical ponderomotive *quiver radius*,[12]

$$\alpha_0 = \frac{e\mathcal{E}_0}{m\omega_0^2}, \tag{31}$$

which is the classical turning point for the excursion of the electron in the presence of the field. For field parameters $\mathcal{E}_0$ = 0.05 a.u. and $\hbar\omega_0$ = 1.55 eV (corresponding to $I = 10^{14}$ W/cm^2), Eq. (31) affords α_0 = 15.4 a_0. This is well outside of the CAP radius r_0 = 9.525 a_0 that is used in Figs. 9(a) and 9(b) although it is inside of the larger CAP radius (r_0 = 18.5 a_0) that is used in Figs. 9(c) and 9(d). In view of this, it is perhaps not surprising that the smaller CAP radius attenuates the harmonic sequences earlier as compared to the larger radius although from another point of view, it is surprising that so much of the harmonic progression can be resolved using a value $r_0 < \alpha_0$. It should be noted that a CAP is an imperfect absorber,[53,76] and it must be the case that even with r_0 = 9.524 a_0, the wave packet experiences sufficient field cycles within the envelope of the CAP in order to generate a non-trivial number of harmonics, if not the full progression. (For r_0 = 4.0 a_0, this is clearly not the case.) Future work might try to visualize the wave packet to understand how much of it survives at the classical turning point.

C. Windowing technique

Focusing now on the spectrum with CAP parameters r_0 = 18.5 a_0 and η = 0.1 E_h/a_0^2 [Fig. 9(d)], we next present several

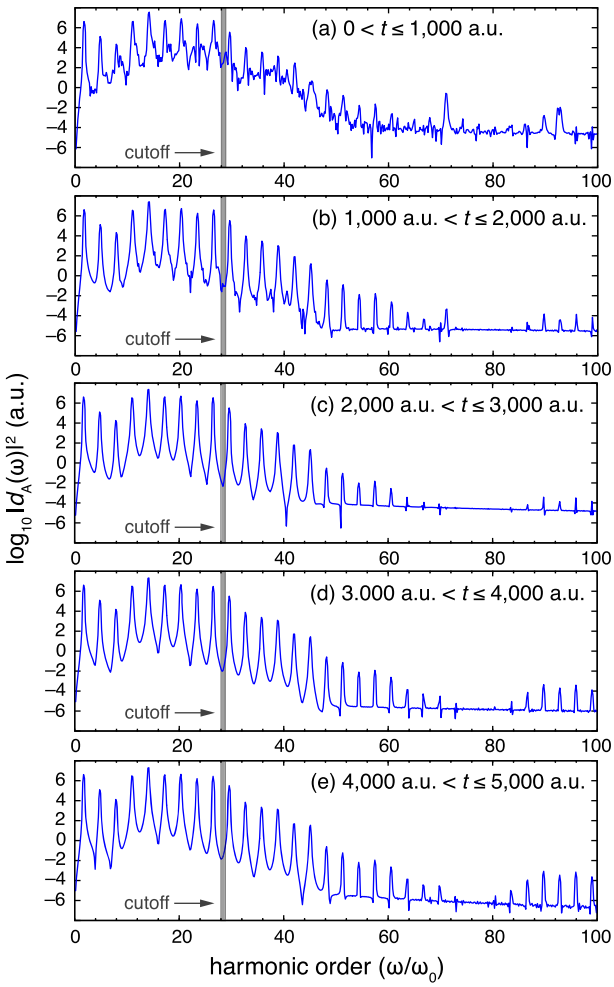

FIG. 11. HHG spectra for H_2 computed at the TDHF/5-aTZ level from a continuous-wave simulation with CAP parameters r_0 = 18.5 a_0 and η = 0.1 E_h/a_0^2, as in Fig 9(d). The total simulation time of 5000 a.u. has been divided into consecutive segments, and the spectra in (a)–(e) are obtained from the Fourier transform of the $\mu_z(t)$ data within just one segment, as indicated. The logarithmic intensity scale is the same in each panel, and the semiclassical cutoff [Eq. (7)] is indicated.

versions of this spectrum computed from the same simulation data via "windowed" Fourier transforms. In Fig. 11, the total simulation time of 5000 a.u. has been divided into five sequential segments and the transform is computed separately within each segment. For the segment corresponding to $0 < t \leq 1000$ a.u. [Fig. 11(a)], peaks are obtained at the odd harmonic numbers but they are not yet very clear or sharp, with considerable noise in the spectrum and no clear indication of where the harmonic progression terminates. Within the second data segment [Fig. 11(b)], corresponding to the subsequent 1000 a.u. of simulation data, peaks become much sharper although some noise remains. A drop in intensity at the semiclassical cutoff value [Eq. (7)] becomes more apparent, and it is clear that the harmonic progression terminates at or near the 72nd harmonic. The noise largely disappears in the third data segment, corresponding to 2000 a.u. $< t \leq 3000$ a.u., and subsequent data segments afford little change in the HHG spectrum. In view of this information, we could have propagated the continuous-wave simulations for 3000 a.u. rather than 5000 a.u. and obtained a spectrum of similar quality from the final one-third of the shorter simulation. Results in Fig. S8 demonstrate that this windowing procedure also cleans up the spectrum when the CAP radius is set to the much smaller value $r_0 = 9.524\ a_0$, even if the harmonic progression is terminated prematurely under those conditions.

This windowing procedure is important for extending the present methodology to larger polyatomic molecules, and its success can be interpreted as follows. In the hypothetical case that the basis set were complete and covered all of space, extending to infinity, then some part of the H_2 wave packet would quickly be ionized by the strong laser field, never to return. In practice, the finite extent of the basis functions means that there are spurious peaks corresponding to excitations into unbound states and the most significant spurious features coincide with excited states having nonzero oscillator strength. Other noise is generated by a partially reflected wave. By windowing the spectrum, we only include $\mu(t)$ data from later times in the Fourier transform, by which time some of the high-frequency, artificially trapped electron wave has been absorbed by the CAP.

V. SUMMARY AND CONCLUSIONS

We have examined the calculation of high-harmonic spectra using TDKS simulations (otherwise known as "real-time" TDDFT) using atom-centered Gaussian basis functions and an atom-centered, real-space CAP based on a new implementation of the TDKS method in the Q-Chem software.[34,93] In these strong-field simulations, the CAP serves to absorb the highest-energy part of the outgoing electronic wave packet, which would otherwise reflect off of the artificial barrier that is created by the finite extent of the basis set. Interference between the outgoing and reflected waves then leads to significant noise in the high harmonic spectrum that is obtained from the fluctuating dipole moment function.

In this preliminary report, we have characterized the CAP parameters that are needed to obtain a well-defined harmonic progression in agreement with grid-based TDKS simulations. In the absence of the CAP, only a few low-energy harmonics are obtained, but even with the CAP turned on the results are sensitive to the values of the turn-on radius (r_0). A value of r_0 that is smaller than the semiclassical quiver radius (α_0) results in premature attenuation of the harmonic progression, although perhaps surprisingly, a long sequence of harmonics can still be observed even when $r_0 < \alpha_0$. The value of the CAP strength parameter (η) affects the background noise to some extent, although the results are less strongly dependent on this parameter.

The use of atom-centered basis functions, along with a commensurate atom-centered CAP that can be represented using standard atom-centered quadrature grids (as used routinely in DFT calculations[92]) makes the present methodology much more extensible to larger molecular systems as compared to grid-based solution of the TDKS equations. The cost of a single TDKS time step is comparable to the cost of a ground-state SCF cycle, and the memory footprint is only twice that of a ground-state DFT calculation (because the matrices are complex-valued). The Gaussian orbital representation is thus essential for extending strong-field calculations to larger systems, and others have already reported the applications of the Gaussian-based TDKS approach to polyatomic molecules including the HHG spectra of CH_2Cl_2 and strong-field ionization rates of C_6H_8, both at the TD-CIS level.[77,102] The present work suggests an efficient means to add correlation to those calculations, as an alternative to time-dependent implementations of correlated wave function models.[30] In moving to larger systems, one may need to deal with a linear dependency problem arising when very diffuse basis sets are employed, which we circumvent in the present work using tight thresholds. As in the case of weakly bound anions,[71] judicious use of floating centers ("ghost atoms"), or augmentation of selected atoms only, may help to circumvent this problem in larger molecules. This extensibility may open the door to simulations of strong-field phenomena in a wide variety of complex systems.

SUPPLEMENTARY MATERIAL

See the supplementary material for additional calculations and convergence tests.

ACKNOWLEDGMENTS

This work was supported by the National Science Foundation under Grant Nos. CHE-1665322 and CHE-1955282. Calculations were performed at the Ohio Supercomputer Center.[103]

AUTHOR DECLARATIONS

Conflict of Interest

J.M.H. serves on the board of directors of Q-Chem, Inc.

DATA AVAILABILITY

The data that support the findings of this study are available from the corresponding author upon reasonable request.

REFERENCES

[1] F. Krausz and M. Ivanov, "Attosecond physics," Rev. Mod. Phys. **81**, 163–234 (2009).

[2] K. L. Ishikawa, "High-harmonic generation," in *Advances in Solid State Lasers: Development and Applications*, edited by M. Grishin (IntechOpen, Croatia, 2010).

[3] T. Popmintchev, M.-C. Chen, D. Popmintchev, P. Arpin, S. Brown, S. Ališauskas, G. Andriukaitis, T. Balčiunas, O. D. Mücke, A. Pugzlys, A. Baltuška, B. Shim, S. E. Schrauth, A. Gaeta, C. Hernández-García, L. Plaja, A. Becker, A. Jaron-Becker, M. M. Murnane, and H. C. Kapteyn, "Bright coherent ultrahigh harmonics in the keV x-ray regime from mid-infrared femtosecond lasers," Science **336**, 1287–1291 (2012).

[4] A. S. Johnson, T. Avni, E. W. Larsen, D. R. Austin, and J. P. Marangos, "Attosecond soft X-ray high harmonic generation," Philos. Trans. R. Soc., A **377**, 20170468 (2019).

[5] L. Miaja-Avila, G. C. O'Neil, J. Uhlig, C. L. Cromer, M. L. Dowell, R. Jimenez, A. S. Hoover, K. L. Silverman, and J. N. Ullom, "Laser plasma x-ray source for ultrafast time-resolved x-ray absorption spectroscopy," Struct. Dyn. **2**, 024301 (2015).

[6] R. Schoenlein, T. Elsaesser, K. Holldack, Z. Huang, H. Kapteyn, M. Murnane, and M. Woerner, "Recent advances in ultrafast X-ray sources," Philos. Trans. R. Soc., A **377**, 20180384 (2019).

[7] R. Geneaux, H. J. B. Marroux, A. Guggenmos, D. M. Neumark, and S. R. Leone, "Transient absorption spectroscopy using high harmonic generation: A review of ultrafast X-ray dynamics in molecules and solids," Philos. Trans. R. Soc., A **377**, 20170463 (2019).

[8] A. Depresseux, E. Oliva, J. Gautier, F. Tissandier, J. Nejdl, M. Kozlova, G. Maynard, J. P. Goddet, A. Tafzi, A. Lifschitz, H. T. Kim, S. Jacquemot, V. Malka, K. Ta Phuoc, C. Thaury, P. Rousseau, G. Iaquaniello, T. Lefrou, A. Flacco, B. Vodungbo, G. Lambert, A. Rousse, P. Zeitoun, and S. Sebban, "Table-top femtosecond X-ray laser by collisional ionization gating," Nat. Photonics **9**, 817–822 (2015).

[9] C. Kleine, M. Ekimova, G. Goldsztejn, S. Raabe, C. Strüber, J. Ludwig, S. Yarlagadda, S. Eisebitt, M. J. J. Vrakking, T. Elsaesser, E. T. J. Nibbering, and A. Rouzée, "Soft X-ray absorption spectroscopy of aqueous solutions using a table-top femtosecond soft X-ray source," J. Phys. Chem. Lett. **10**, 52–58 (2019).

[10] A. D. Smith, T. Balčiūnas, Y.-P. Chang, C. Schmidt, K. Zinchenko, F. B. Nunes, E. Rossi, V. Svoboda, Z. Yin, J.-P. Wolf, and H. J. Wörner, "Femtosecond soft-X-ray absorption spectroscopy of liquids with a water-window high-harmonic source," J. Phys. Chem. Lett. **11**, 1981–1988 (2020).

[11] L. F. DiMauro and P. Agostini, "Ionization dynamics in strong laser fields," in *Advances in Atomic, Molecular, and Optical Physics*, edited by B. Bederson and H. Walther (Academic Press, San Diego, 1995), Vol. 35, pp. 79–120.

[12] C. J. Joachain, N. J. Kylstra, and R. M. Potvliege, *Atoms in Intense Laser Fields* (Cambridge University Press, 2012).

[13] F. Lépine, "Short-pulse physics," in *Fundamentals of Time-Dependent Density Functional Theory*, Lecture Notes in Physics Vol. 837, edited by M. A. L. Marques, N. T. Maitra, F. M. S. Nogueira, E. K. U. Gross, and A. Rubio (Springer-Verlag, Berlin, 2012), Chap. 1, pp. 3–14.

[14] C. A. Ullrich and A. D. Bandrauk, "Atoms and molecules in strong laser fields," in *Fundamentionals of Time-Dependent Density Functional Theory*, Lecture Notes in Physics Vol. 837, edited by M. A. L. Marques, N. T. Maitra, F. M. S. Nogueira, E. K. U. Gross, and A. Rubio (Springer-Verlag, Berlin, 2012), Chap. 18, pp. 351–371.

[15] M. Nisoli, P. Decleva, F. Calegari, A. Palacios, and F. Martín, "Attosecond electron dynamics in molecules," Chem. Rev. **117**, 10760–10825 (2017).

[16] K. Ramasesha, S. R. Leone, and D. M. Neumark, "Real-time probing of electron dynamics using attosecond time-resolved spectroscopy," Annu. Rev. Phys. Chem. **67**, 41–63 (2016).

[17] A. Jaroń-Becker and A. Becker, "Attosecond spectroscopy," in *Encyclopedia of Modern Optics*, edited by B. D. Guenther and D. G. Steel, 2nd ed. (Elsevier, Amsterdam, 2018), Vol. 2, pp. 233–243.

[18] L. S. Cederbaum and J. Zobeley, "Ultrafast charge migration by electron correlation," Chem. Phys. Lett. **307**, 205–210 (1999).

[19] A. I. Kuleff, N. V. Kryzhevoi, M. Pernpointner, and L. S. Cederbaum, "Core ionization initiates subfemtosecond charge migration in the valence shell of molecules," Phys. Rev. Lett. **117**, 093002 (2016).

[20] P. M. Kraus and H. J. Wörner, "Perspectives of attosecond spectroscopy for the understanding of fundamental electron correlations," Angew. Chem., Int. Ed. **57**, 5228–5247 (2018).

[21] A. S. Folorunso, A. Bruner, F. Mauger, K. A. Hamer, S. Hernandez, R. R. Jones, L. F. DiMauro, M. B. Gaarde, K. J. Schafer, and K. Lopata, "Molecular modes of attosecond charge migration," Phys. Rev. Lett. **126**, 133002 (2021).

[22] A. Palacios and F. Martín, "The quantum chemistry of attosecond molecular science," Wiley Interdiscip. Rev.: Comput. Mol. Sci. **10**, e1430 (2020).

[23] E. Coccia and E. Luppi, "Time-dependent *ab initio* approaches for high-harmonic generation spectroscopy," J. Phys.: Condens. Matter **34**, 073001 (2022).

[24] E. K. U. Gross, C. A. Ullrich, and U. J. Gossmann, "Density functional theory of time-dependent systems," in *Density Functional Theory*, edited by E. K. U. Gross and R. M. Dreizler (Plenum Press, New York, 1995), pp. 149–171.

[25] E. K. U. Gross and N. T. Maitra, "Introduction to TDDFT," in *Fundamentals of Time-Dependent Density Functional Theory*, Lecture Notes in Physics Vol. 837, edited by M. A. L. Marques, N. T. Maitra, F. M. S. Nogueira, E. K. U. Gross, and A. Rubio (Springer-Verlag, Heidelberg, 2012), Chap. 1, pp. 53–97.

[26] C. Ullrich, *Time-Dependent Density-Functional Theory: Concepts and Applications* (Oxford University Press, New York, 2012).

[27] F. Furche, "On the density matrix based approach to time-dependent density functional response theory," J. Chem. Phys. **114**, 5982–5992 (2001).

[28] A. Dreuw and M. Head-Gordon, "Single-reference ab initio methods for the calculation of excited states of large molecules," Chem. Rev. **105**, 4009–4037 (2005).

[29] Y. Kawashita, T. Nakatsukasa, and K. Yabana, "Time-dependent density-functional theory simulation for electron-ion dynamics in molecules under intense laser pulses," J. Phys.: Condens. Matter **21**, 064222 (2009).

[30] X. Li, N. Govind, C. Isborn, A. E. DePrince III, and K. Lopata, "Real-time time-dependent electronic structure theory," Chem. Rev. **120**, 9951–9993 (2020).

[31] M. R. Provorse and C. M. Isborn, "Electron dynamics with real-time time-dependent density functional theory," Int. J. Quantum Chem. **116**, 739–749 (2016).

[32] J. M. Herbert, "Density functional theory for electronic excited states," in Theoretical and Computational Photochemistry: Fundamentals, Methods, Applications and Synergy with Experimental Approaches, edited by C. García-Iriepa and M. Marazzi (Elsevier, 2022), Chap. 3; arXiv.2204.10135.

[33] Y. Zhu and J. M. Herbert, "Self-consistent predictor/corrector algorithms for stable and efficient integration of the time-dependent Kohn-Sham equation," J. Chem. Phys. **148**, 044117 (2018).

[34] Y. Zhu, B. Alam, and J. M. Herbert, "Broadband X-ray absorption spectra from time-dependent Kohn-Sham calculations," chemRxiv:14766960.v1 (2021).

[35] M. Lein and S. Kümmel, "Exact time-dependent exchange-correlation potentials for strong-field electron dynamics," Phys. Rev. Lett. **94**, 143003 (2005).

[36] X. Chu and P. J. Memoli, "Role of multiphoton excitation and two-electron effects in high harmonic generation of H_2: A TDDFT calculation," Chem. Phys. **391**, 83–87 (2011).

[37] X. Chu and G. C. Groenenboom, "Time-dependent density-functional-theory calculation of high-order-harmonic generation of H_2," Phys. Rev. A **85**, 053402 (2012).

[38] F. Bedurke, T. Klamroth, and P. Saalfrank, "Many-electron dynamics in laser-driven molecules: Wavefunction theory vs density functional theory," Phys. Chem. Chem. Phys. **23**, 13544–13560 (2021).

[39] E. Luppi and M. Head-Gordon, "Computation of high-harmonic generation spectra of H_2 and N_2 in intense laser pulses using quantum chemistry methods and time-dependent density functional theory," Mol. Phys. **110**, 909–923 (2012).

[40] S. Klinkusch, P. Saalfrank, and T. Klamroth, "Laser-induced electron dynamics including photoionization: A heuristic model within time-dependent configuration interaction theory," J. Chem. Phys. **131**, 114304 (2009).

[41] A. F. White, C. J. Heide, P. Saalfrank, M. Head-Gordon, and E. Luppi, "Computation of high-harmonic generation spectra of the hydrogen molecule using time-dependent configuration-interaction," Mol. Phys. **114**, 947–956 (2016).
[42] C. F. Pauletti, E. Coccia, and E. Luppi, "Role of exchange and correlation in high-harmonic generation spectra of H_2, N_2, and CO_2: Real-time time-dependent electronic structure approaches," J. Chem. Phys. **154**, 014101 (2021).
[43] H. Iikura, T. Tsuneda, T. Yanai, and K. Hirao, "A long-range correction scheme for generalized-gradient-approximation exchange functionals," J. Chem. Phys. **115**, 3540–3544 (2001).
[44] M. A. Rohrdanz and J. M. Herbert, "Simultaneous benchmarking of ground- and excited-state properties with long-range-corrected density functional theory," J. Chem. Phys. **129**, 034107 (2008).
[45] A. W. Lange, M. A. Rohrdanz, and J. M. Herbert, "Charge-transfer excited states in a π-stacked adenine dimer, as predicted using long-range-corrected time-dependent density functional theory," J. Phys. Chem. B **112**, 6304–6308 (2008); Erratum **112**, 7345 (2008).
[46] M. A. Rohrdanz, K. M. Martins, and J. M. Herbert, "A long-range-corrected density functional that performs well for both ground-state properties and time-dependent density functional theory excitation energies, including charge-transfer excited states," J. Chem. Phys. **130**, 054112 (2009).
[47] R. M. Richard and J. M. Herbert, "Time-dependent density-functional description of the ^1L_a state in polycyclic aromatic hydrocarbons: Charge-transfer character in disguise?," J. Chem. Theory Comput. **7**, 1296–1306 (2011).
[48] B. Alam, A. F. Morrison, and J. M. Herbert, "Charge separation and charge transfer in the low-lying excited states of pentacene," J. Phys. Chem. C **124**, 24653–24666 (2020).
[49] A. Sissay, P. Abanador, F. Mauger, M. Gaarde, K. J. Schafer, and K. Lopata, "Angle-dependent strong-field molecular ionization rates with tuned range-separated time-dependent density functional theory," J. Chem. Phys. **145**, 094105 (2016).
[50] P. Sándor, A. Sissay, F. Mauger, P. M. Abanador, T. T. Gorman, T. D. Scarborough, M. B. Gaarde, K. Lopata, K. J. Schafer, and R. R. Jones, "Angle dependence of strong-field single and double ionization of carbonyl sulfide," Phys. Rev. A **98**, 043425 (2018).
[51] O. A. Vydrov, G. E. Scuseria, and J. P. Perdew, "Tests of functionals for systems with fractional electron number," J. Chem. Phys. **126**, 154109 (2007).
[52] F. L. Yip, C. W. McCurdy, and T. N. Rescigno, "Hybrid Gaussian–discrete-variable representation for one- and two-active-electron continuum calculations in molecules," Phys. Rev. A **90**, 063421 (2014).
[53] S. Pabst, A. Sytcheva, O. Geffert, and R. Santra, "Stability of the time-dependent configuration-interaction-singles method in the attosecond and strong-field regimes: A study of basis set and absorption methods," Phys. Rev. A **94**, 033421 (2016).
[54] M. Ruberti, P. Decleva, and V. Averbukh, "Multi-channel dynamics in high harmonic generation of aligned CO_2: *Ab initio* analysis with time-dependent B-spline algebraic diagrammatic construction," Phys. Chem. Chem. Phys. **20**, 8311–8325 (2018).
[55] M. Labeye, F. Zapata, E. Coccia, V. Véniard, J. Toulouse, J. Caillat, R. Taïeb, and E. Luppi, "Optimal basis set for electron dynamics in strong laser fields: The case of molecular ion H_2^+," J. Chem. Theory Comput. **14**, 5846–5858 (2018).
[56] E. Luppi and M. Head-Gordon, "The role of Rydberg and continuum levels in computing high harmonic generation spectra of the hydrogen atom using time-dependent configuration interaction," J. Chem. Phys. **139**, 164121 (2013).
[57] E. Coccia, B. Mussard, M. Labeye, J. Caillat, R. Taïeb, J. Toulouse, and E. Luppi, "Gaussian continuum basis functions for calculating high-harmonic generation spectra," Int. J. Quantum Chem. **116**, 1120–1131 (2016).
[58] E. Coccia and E. Luppi, "Detecting the minimum in argon high-harmonic generation using Gaussian basis sets," Theor. Chem. Acc. **138**, 96 (2019).
[59] C. Witzorky, G. Paramonov, F. Bouakline, R. Jaquet, P. Saalfrank, and T. Klamroth, "Gaussian-type orbital calculations for high harmonic generation in vibrating molecules: Benchmarks for H_2^+," J. Chem. Theory Comput. **17**, 7353–7365 (2021).
[60] T. T. Luu, Z. Yin, A. Jain, T. Gaumnitz, Y. Pertot, J. Ma, and H. J. Wörner, "Extreme-ultraviolet high-harmonic generation in liquids," Nat. Commun. **9**, 3723 (2018).
[61] S. Ghimire, A. D. DiChiara, E. Sistrunk, P. Agostini, L. F. DiMauro, and D. A. Reis, "Observation of high-order harmonic generation in a bulk crystal," Nat. Phys. **7**, 138–141 (2011).
[62] S. Han, H. Kim, Y. W. Kim, Y.-J. Kim, S. Kim, I.-Y. Park, and S.-W. Kim, "High-harmonic generation by field enhanced femtosecond pulses in metal-sapphire nanostructure," Nat. Commun. **7**, 13105 (2016).
[63] M. F. Ciappina, J. A. Pérez-Hernández, A. S. Landsman, W. A. Okell, S. Zherebtsov, B. Förg, J. Schötz, L. Seiffert, T. Fennel, T. Shaaran, T. Zimmermann, A. Chacón, R. Guichard, A. Zaïr, J. W. G. Tisch, J. P. Marangos, T. Witting, A. Braun, S. A. Maier, L. Roso, M. Krüger, P. Hommelhoff, M. F. Kling, F. Krausz, and M. Lewenstein, "Attosecond physics at the nanoscale," Rep. Prog. Phys. **80**, 054401 (2017).
[64] H. Liu, C. Guo, G. Vampa, J. L. Zhang, T. Sarmiento, M. Xiao, P. H. Bucksbaum, J. Vučković, S. Fan, and D. A. Reis, "Enhanced high-harmonic generation from all-dielectric metasurface," Nat. Phys. **14**, 1006–1010 (2018).
[65] D. Franz, S. Kaassamani, D. Gauthier, R. Nicolas, M. Kholodtsova, L. Douillard, J.-T. Gomes, L. Lavoute, D. Gaponov, N. Ducros, S. Février, J. Biegert, L. Shi, M. Kovacev, W. Boutu, and H. Merdji, "All semiconductor enhanced high-harmonic generation from a single nanostructured cone," Sci. Rep. **9**, 5663 (2019).
[66] A.-W. Zeng and X.-B. Bian, "Impact of statistical fluctuations on high harmonic generation in liquids," Phys. Rev. Lett. **124**, 203901 (2020).
[67] X. Chu and G. C. Groeneboom, "Contributions of inner-valence molecular orbitals and multiphoton resonances to high-order-harmonic generation of N_2: A time-dependent density-functional-theory study," Phys. Rev. A **93**, 013422 (2016).
[68] M. Lewenstein, P. Balcou, M. Y. Ivanov, A. L'Huillier, and P. B. Corkum, "Theory of high-harmonic generation by low-frequency laser fields," Phys. Rev. A **49**, 2117–2132 (1994).
[69] E. Coccia, R. Assaraf, E. Luppi, and J. Toulouse, "*Ab initio* lifetime correction to scattering states for time-dependent electronic-structure calculations with incomplete basis sets," J. Chem. Phys. **147**, 014106 (2017).
[70] S. Klaiman and I. Gilary, "On resonance: A first glance in the behavior of unstable states," Adv. Quantum Chem. **63**, 1–31 (2012).
[71] J. M. Herbert, "The quantum chemistry of loosely-bound electrons," in *Reviews in Computational Chemistry*, edited by A. L. Parill and K. Lipkowitz (Wiley VCH, Hoboken, NJ, 2015), Vol. 28, Chap. 8, pp. 391–517.
[72] T.-C. Jagau, K. B. Bravaya, and A. I. Krylov, "Extending the quantum chemistry of bound states to electronic resonances," Annu. Rev. Phys. Chem. **68**, 525–553 (2017).
[73] U. V. Riss and H. D. Meyer, "Investigation on the reflection and transmission properties of complex absorbing potentials," J. Chem. Phys. **105**, 1409–1419 (1996).
[74] X. Chu, "Time-dependent density-functional-theory calculation of strong-field ionization rates of H_2," Phys. Rev. A **82**, 023407 (2010).
[75] X. Chu and G. C. Groenboom, "Role of resonance-enhanced multiphoton excitation in high-harmonic generation of N_2: A time-dependent density-functional-theory study," Phys. Rev. A **87**, 013434 (2013).
[76] A. Karamatskou, S. Pabst, Y.-J. Chen, and R. Santra, "Calculation of photoelectron spectra within the time-dependent configuration-interaction singles scheme," Phys. Rev. A **89**, 033415 (2014).
[77] P. Krause and H. B. Schlegel, "Strong field ionization rates of linear polyenes simulated with time-dependent configuration interaction and an absorbing potential," J. Chem. Phys. **141**, 174104 (2014).
[78] P. Krause, J. A. Sonk, and H. B. Schlegel, "Strong field ionization rates simulated with time-dependent configuration interaction and an absorbing potential," J. Chem. Phys. **140**, 174113 (2014).
[79] P. Krause and H. B. Schlegel, "Angle-dependent ionization of small molecules by time-dependent configuration interaction and an absorbing potential," J. Phys. Chem. Lett. **6**, 2140–2146 (2015).
[80] P. Krause and H. B. Schlegel, "Angle-dependent ionization of hydrides AH_n calculated by time-dependent configuration interaction with an absorbing potential," J. Phys. Chem. A **119**, 10212–10220 (2015).

[81] P. Hoerner and H. B. Schlegel, "Angular dependence of ionization by circularly polarized light calculated with time-dependent configuration interaction with an absorbing potential," J. Phys. Chem. A **121**, 1336–1343 (2017).
[82] P. Hoerner, W. Li, and H. B. Schlegel, "Angular dependence of strong field ionization of 2-phenylethyl-*N*,*N*-dimethylamine (PENNA) using time-dependent configuration interaction with an absorbing potential," J. Phys. Chem. A **124**, 4777–4781 (2020).
[83] P. Hoerner and H. B. Schlegel, "Angular dependence of strong field ionization of haloacetylenes HCCX (X = F, Cl, Br, I) using time-dependent configuration interaction with an absorbing potential," J. Phys. Chem. C **122**, 13751–13757 (2018).
[84] P. Hoerner and H. B. Schlegel, "Angular dependence of strong field ionization of CH_3X (X = F, Cl, Br, or I) using time-dependent configuration interaction with an absorbing potential," J. Phys. Chem. A **121**, 5940–5946 (2017).
[85] P. Hoerner, W. Li, and H. B. Schlegel, "Sequential double ionization of molecules by strong laser fields simulated with time-dependent configuration interaction," J. Chem. Phys. **155**, 114103 (2021).
[86] M. K. Lee, P. Hoerner, W. Li, and H. B. Schlegel, "Effect of spin–orbit coupling on strong field ionization simulated with time-dependent configuration interaction," J. Chem. Phys. **153**, 244109 (2020).
[87] J. L. Krause, K. J. Schafer, and K. C. Kulander, "High-order harmonic generation from atoms and ions in the high intensity regime," Phys. Rev. Lett. **68**, 3535–3538 (1992).
[88] K. J. Schafer, B. Yang, L. F. DiMauro, and K. C. Kulander, "Above threshold ionization beyond the high harmonic cutoff," Phys. Rev. Lett. **70**, 1599–1602 (1993).
[89] D.-S. Guo, C. Yu, J. Zhang, J. Gao, Z.-W. Sun, and Z. Sun, "On the cutoff law of laser induced high harmonic spectra," Front. Phys. **10**, 209–214 (2015).
[90] C. Leforestier, R. H. Bisseling, C. Cerjan, M. D. Feit, R. Friesner, A. Guldberg, A. Hammerich, G. Jolicard, W. Karrlein, H.-D. Meyer, N. Lipkin, O. Roncero, and R. Kosloff, "A comparison of different propagation schemes for the time dependent Schrödinger equation," J. Comput. Phys. **94**, 59–80 (1991).
[91] X. Li, S. M. Smith, A. N. Markevitch, D. A. Romanov, R. J. Levis, and H. B. Schlegel, "A time-dependent Hartree–Fock approach for studying the electronic optical response of molecules in intense fields," Phys. Chem. Chem. Phys. **7**, 233–239 (2005).
[92] S. Dasgupta and J. M. Herbert, "Standard grids for high-precision integration of modern density functionals: SG-2 and SG-3," J. Comput. Chem. **38**, 869–882 (2017).
[93] E. Epifanovsky, A. T. B. Gilbert, X. Feng, J. Lee, Y. Mao, N. Mardirossian, P. Pokhilko, A. F. White, M. P. Coons, A. L. Dempwolff, Z. Gan, D. Hait, P. R. Horn, L. D. Jacobson, I. Kaliman, J. Kussmann, A. W. Lange, K. U. Lao, D. S. Levine, J. Liu, S. C. McKenzie, A. F. Morrison, K. D. Nanda, F. Plasser, D. R. Rehn, M. L. Vidal, Z.-Q. You, Y. Zhu, B. Alam, B. J. Albrecht, A. Aldossary, E. Alguire, J. H. Andersen, V. Athavale, D. Barton, K. Begam, A. Behn, N. Bellonzi, Y. A. Bernard, E. J. Berquist, H. G. A. Burton, A. Carreras, K. Carter-Fenk, R. Chakraborty, A. D. Chien, K. D. Closser, V. Cofer-Shabica, S. Dasgupta, M. de Wergifosse, J. Deng, M. Diedenhofen, H. Do, S. Ehlert, P.-T. Fang, S. Fatehi, Q. Feng, T. Friedhoff, J. Gayvert, Q. Ge, G. Gidofalvi, M. Goldey, J. Gomes, C. E. González-Espinoza, S. Gulania, A. O. Gunina, M. W. D. Hanson-Heine, P. H. P. Harbach, A. Hauser, M. F. Herbst, M. Hernández Vera, M. Hodecker, Z. C. Holden, S. Houck, X. Huang, K. Hui, B. C. Huynh, M. Ivanov, Á. Jász, H. Ji, H. Jiang, B. Kaduk, S. Kähler, K. Khistyaev, J. Kim, G. Kis, P. Klunzinger, Z. Koczor-Benda, J. H. Koh, D. Kosenkov, L. Koulias, T. Kowalczyk, C. M. Krauter, K. Kue, A. Kunitsa, T. Kus, I. Ladjánszki, A. Landau, K. V. Lawler, D. Lefrancois, S. Lehtola, R. R. Li, Y.-P. Li, J. Liang, M. Liebenthal, H.-H. Lin, Y.-S. Lin, F. Liu, K.-Y. Liu, M. Loipersberger, A. Luenser, A. Manjanath, P. Manohar, E. Mansoor, S. F. Manzer, S.-P. Mao, A. V. Marenich, T. Markovich, S. Mason, S. A. Maurer, P. F. McLaughlin, M. F. S. J. Menger, J.-M. Mewes, S. A. Mewes, P. Morgante, J. W. Mullinax, K. J. Oosterbaan, G. Paran, A. C. Paul, S. K. Paul, F. Pavošević, Z. Pei, S. Prager, E. I. Proynov, Á. Rák, E. Ramos-Cordoba, B. Rana, A. E. Rask, A. Rettig, R. M. Richard, F. Rob, E. Rossomme, T. Scheele, M. Scheurer, M. Schneider, N. Sergueev, S. M. Sharada, W. Skomorowski, D. W. Small, C. J. Stein, Y.-C. Su, E. J. Sundstrom, Z. Tao, J. Thirman, G. J. Tornai, T. Tsuchimochi, N. M. Tubman, S. P. Veccham, O. Vydrov, J. Wenzel, J. Witte, A. Yamada, K. Yao, S. Yeganeh, S. R. Yost, A. Zech, I. Y. Zhang, X. Zhang, Y. Zhang, D. Zuev, A. Aspuru-Guzik, A. T. Bell, N. A. Besley, K. B. Bravaya, B. R. Brooks, D. Casanova, J.-D. Chai, S. Coriani, C. J. Cramer, G. Cserey, A. E. DePrince III, R. A. DiStasio, Jr., A. Dreuw, B. D. Dunietz, T. R. Furlani, W. A. Goddard III, S. Hammes-Schiffer, T. Head-Gordon, W. J. Hehre, C.-P. Hsu, T.-C. Jagau, Y. Jung, A. Klamt, J. Kong, D. S. Lambrecht, W. Liang, N. J. Mayhall, C. W. McCurdy, J. B. Neaton, C. Ochsenfeld, J. A. Parkhill, R. Peverati, V. A. Rassolov, Y. Shao, L. V. Slipchenko, T. Stauch, R. P. Steele, J. E. Subotnik, A. J. W. Thom, A. Tkatchenko, D. G. Truhlar, T. Van Voorhis, T. A. Wesolowski, K. B. Whaley, H. L. Woodcock III, P. M. Zimmerman, S. Faraji, P. M. W. Gill, M. Head-Gordon, J. M. Herbert, and A. I. Krylov, "Software for the frontiers of quantum chemistry: An overview of developments in the Q-Chem 5 package," J. Chem. Phys. **155**, 084801 (2021).
[94] T. S. Nguyen and J. Parkhill, "Nonadiabatic dynamics for electrons at second-order: Real-time TDDFT and OSCF2," J. Chem. Theory Comput. **11**, 2918–2924 (2015).
[95] T. S. Nguyen, J. H. Koh, S. Lefelhocz, and J. Parkhill, "Black-box, real-time simulations of transient absorption spectroscopy," J. Phys. Chem. Lett. **7**, 1590–1595 (2016).
[96] V. P. Krainov, H. R. Reiss, and B. M. Smirnov, *Radiative Processes in Atomic Physics* (John Wiley & Sons, New York, 1997).
[97] D. E. Woon and T. H. Dunning, Jr., "Gaussian basis sets for use in correlated molecular calculations. IV. Calculation of static electrical response properties," J. Chem. Phys. **100**, 2975–2988 (1994).
[98] P. M. W. Gill, B. G. Johnson, and J. A. Pople, "A standard grid for density-functional calculations," Chem. Phys. Lett. **209**, 506–512 (1993).
[99] J. M. Herbert and M. Head-Gordon, "Calculation of electron detachment energies for water cluster anions: An appraisal of electronic structure methods, with application to $(H_2O)_{20}^-$ and $(H_2O)_{24}^-$," J. Phys. Chem. A **109**, 5217–5229 (2005).
[100] K. Kaufmann, W. Baumeister, and M. Jungen, "Universal Gaussian basis sets for an optimum representation of Rydberg and continuum wavefunctions," J. Phys. B: At., Mol. Opt. Phys. **22**, 2223–2240 (1989).
[101] R. Zavin, I. Vorobeichik, and N. Moiseyev, "Motion of wave-packets using the smooth-exterior-scaling complex potential," Chem. Phys. Lett. **288**, 413–417 (1998).
[102] F. Bedurke, T. Klamroth, P. Krause, and P. Saalfrank, "Discriminating organic isomers by high harmonic generation: A time-dependent configuration interaction singles study," J. Chem. Phys. **150**, 234114 (2019).
[103] See http://osc.edu/ark:/19495/f5s1ph73 for Ohio Supercomputer Center.